Attitude control actuator scaling laws for orbiting solar reflectors

Andrea Viale *, Colin McInnes †
James Watt School of Engineering, University of Glasgow, Glasgow G12 8QQ, UK

The rapid evolution of in-orbit manufacturing will enable the fabrication of low-cost, large-scale space structures. In particular, the use of 3D printing technologies will remove traditional payload constraints associated with launch vehicles, due to fairing size and launch loads, thus allowing the construction of larger and lighter structures, such as orbiting solar reflectors. These structures will require efficient attitude control systems, able to provide the necessary torque for maneuvers and to counteract perturbations, such as gravity gradient and solar radiation pressure. In this paper, a top-level overview of actuator performances for orbiting solar reflectors is provided, and scaling laws associated with the required actuator mass and input power are developed. For each class of actuator, upper bounds on the maximum size of the structure which can be effectively controlled are presented. The results can also be extended to other classes of large planar Earth-pointing structures such as solar power satellites, solar sails, or large antennae.

Nomenclature

A	area	r	reflectivity
B	magnetic field	R	radius
β	reflector rotation angle about x axis	ρ	density/areal density
d	slant range	σ	stress
ϵ	zenith angle	t	thickness
η_e	photovoltaic conversion efficiency	τ	time
η_a	fraction of reflector area used for energy conversion	T	torque
ϕ	gimbal angle	ω_w	wheel angular velocity
θ	orbit angle	T_m	motor torque
G	gravitational constant	P	power
h	orbit altitude	Subscripts:	
$\hat{\mathbf{i}}, \hat{\mathbf{j}}, \hat{\mathbf{k}}$	unit vectors	$\square_{cl}$	current loop
I	inertia	$\square_E$	Earth
I_{sp}	specific impulse	$\square_m$	motor
l	reflector side	$\square_o$	orbit
m	mass	$\square_{prop}$	propellant
μ	gravitational parameter	$\square_r$	reflector
n	nondimensional number	$\square_{srp}$	solar radiation pressure
ν	Poisson's ratio	$\square_t$	thruster
ω	angular velocity	$\square_{vr}$	variable reflectivity
p	pressure	$\square_w$	wheel
$P_\odot$	solar constant		
P	power		

*Research Associate; andreaviale@protonmail.com
†James Watt Chair, Professor of Engineering Science; Colin.McInnes@glasgow.ac.uk

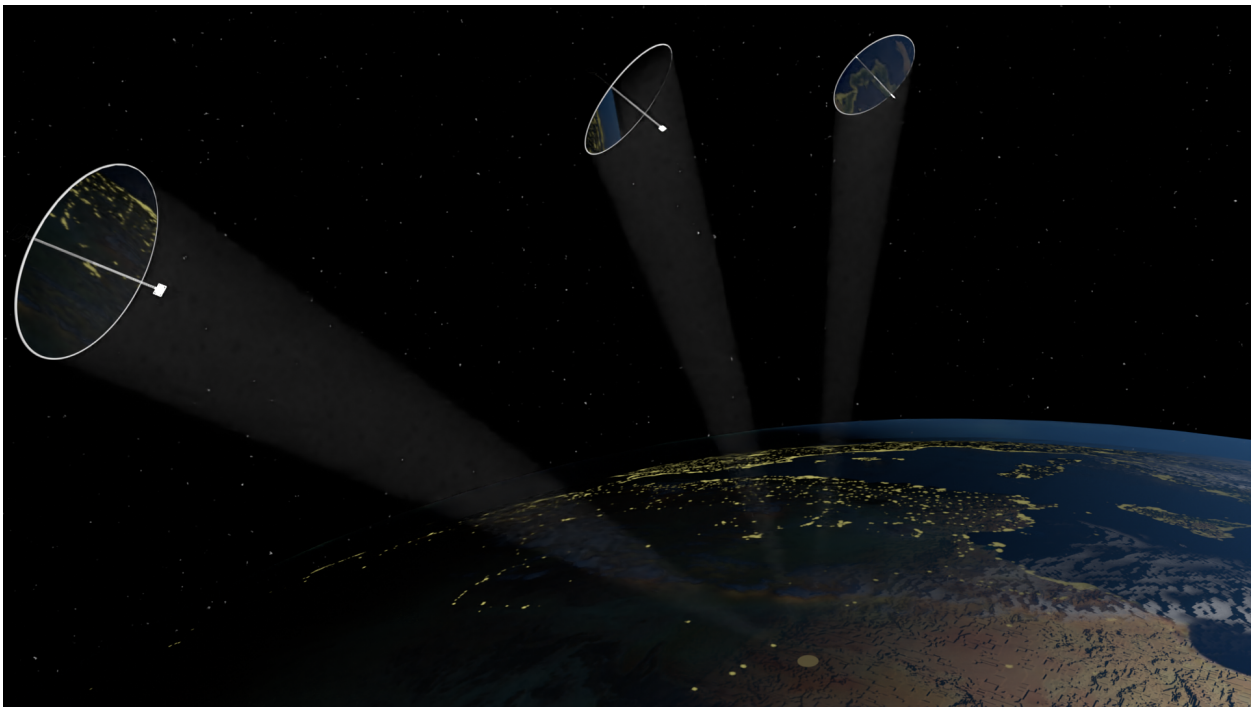

Fig. 1 Representation of a train of mirrors on a polar orbit reflecting sunlight to a solar power farm.

I. Introduction

With the rapid development of in-orbit manufacturing, the possibility of fabricating and assembling low-cost, large-scale space structures will likely become concrete in the coming years [1]. The use of 3D printing technology and robot manipulators will allow the construction of modular lightweight structures without the size constraints typically associated with payloads launched from Earth [2]. Examples of such structures include solar power satellites, orbiting reflectors, antennae and solar sails.

The solar power satellite (SPS) concept is a method proposed to generate solar electricity in orbit and then deliver it to Earth via microwave [3] or laser transmission [4]. For significant power transmission, these structures typically have a large area. For example, a NASA design concept involves a 5 x 15 km structure with a dedicated 8 km diameter ground station [5]. Reference [6] proposes a 3.2 x 3.2 km structure in geostationary orbit controlled by 500 ion thrusters. Orbiting solar reflectors (see Fig. 1) have also been proposed to reflect sunlight to Earth to illuminate terrestrial solar power plants. Contrary to SPS, the mass of the space element is reduced by retaining the power conversion infrastructure on the ground. Sunlight can be reflected to existing solar power farms to enhance their power output during peak energy demand time, such as dawn and dusk, without the need to have a dedicated ground infrastructure, as for the SPS concept [7]. The concept of orbiting solar reflectors was first developed by Oberth in the 1920s, proposing large reflectors in polar orbit for illumination, navigation and enhancing agricultural output [8]. Ehricke then proposed a range of reflector concepts optimized for different applications, such as illumination of rural areas or enhancement of solar energy generation [9]. NASA studies in the 1980s then investigated the performance of a circular reflector with a 1 km diameter in equatorial orbit [10]. Other design strategies include the use of multiple mirrors independently controlled and connected to a larger frame [11]. A comprehensive literature review on orbiting solar reflectors can be found in Ref. [12].

A key requirement for large space structures is the attitude control system. For example, actuators on an orbiting solar reflector must provide torques to continuously slew the structure, such that sunlight is reflected to the desired target. Given the large dimension of such structures, large attitude control torques are expected. In fact, the inertia of a planar structure scales as the product between its mass m and the square of its length l and so for a fixed areal density ρ, as the fourth power of the length l^4. NASA explored the use of large deployable control moment gyroscopes (CMGs) to control a 1 km diameter structure [10]. In particular a design with a pair of 40 meter diameter glass fiber CMGs is proposed, coupled with magnetorquers for desaturation of the wheels. Authors in Refs. [13, 14] proposed

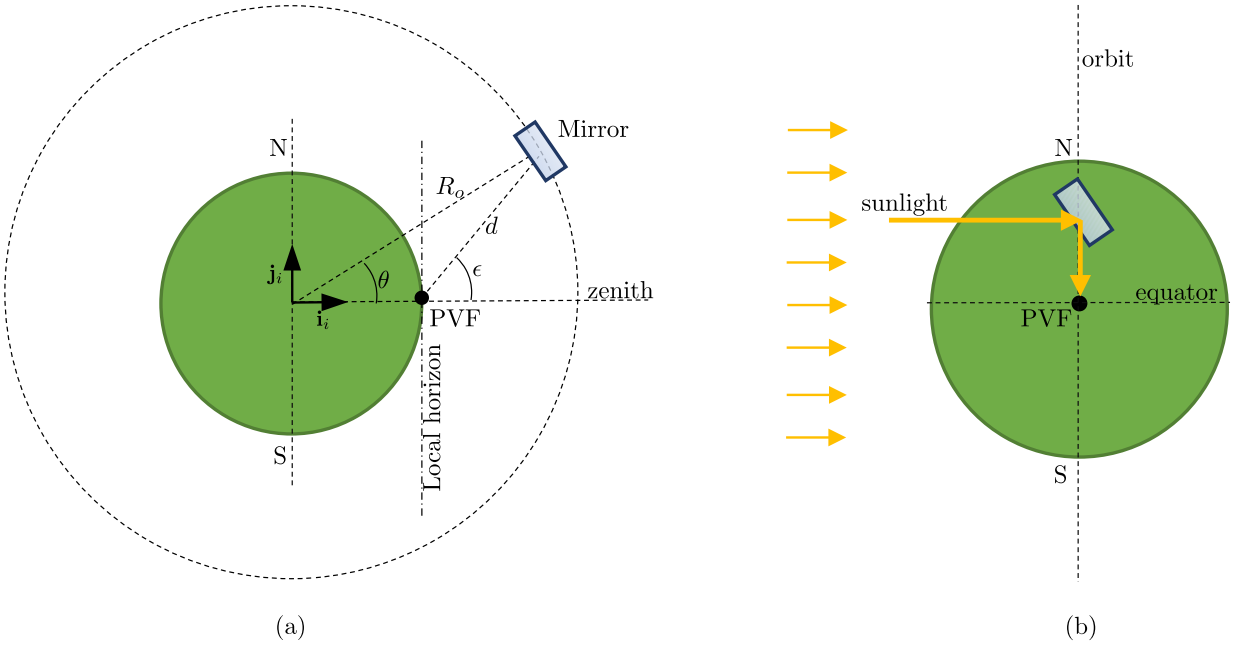

Fig. 2 Orbit geometry, looking towards the orbital plane (a) and the PVF (b).

the used of a distributed array of CMGs primarily for vibration suppression and shape control rather than active slewing of the structure. Similarly, use of piezo-ceramic actuators has been proposed for control of elastic vibrations on large space structures [15]. Authors in Refs.[16, 17] propose to use an array of magnetorquers integrated within the structure capable of providing torque about all three body axes. It is shown that distributed actuators may reduce structural stresses and deformation compared to non-distributed actuators, providing centralized torques. The use of solar radiation pressure (SRP) has also been proposed for control of large structures, in particular solar sails. The most common SRP-based control methods include controllable rotating vanes [18, 19] and sliding masses [20] to change the displacement between the centre-of-mass and the centre-of-pressure. More recently, use of electro-active materials able to change their reflectivity according to an electric potential has been proposed. Authors in Ref. [21] discuss the use of a distributed array of such variable reflectivity cells to generate control torques.

In this paper, simple scaling laws are presented, describing the variation of the required actuator mass and input power as a function of the structure size and operational altitude. The aim is to provide a clear and intuitive understanding of the performances of different classes of actuator (e.g., momentum exchange devices, solar radiation pressure methods, current loops and thrusters) for orbiting solar reflectors, although results can be extended to other classes of Earth-pointing large planar structures (such as SPS, solar sails or large antennae). Moreover, upper bounds on the structure size which is controllable by each actuator are presented, based on the maximum available power or torque constraints.

The paper is organized as follows. The problem statement and orbit geometry is presented in Section II. In Section III the angular acceleration tracking and reorientation requirements are defined and compared with the perturbations due to disturbance torques. Thereafter, Section IV discusses the performances of different classes of actuators, based on their required mass and power. A discussion of the results will follow in Section V.

II. Problem statement and orbital relationships

The geometry of the problem is shown in Fig. 2. A reflector is assumed to be orbiting the Earth on a dawn-dusk circular polar orbit with orbit altitude h and radius $R_o = h + R_E$, where $R_E = 6378\,\text{km}$ is the radius of the Earth. The reflector's attitude control system must ensure constant sunlight reflection to a photovoltaic farm (PVF) located at the Earth's equator when the reflector is above the local horizon note that results for non-equatorial PVFs will be the same due to the symmetry of the problem. The reflector is modeled as a rigid square plate with negligible thickness, side length l and areal density ρ_r. Throughout this paper a constant areal density $\rho_r = 10\,\text{g}\,\text{m}^{-2}$ is chosen, corresponding

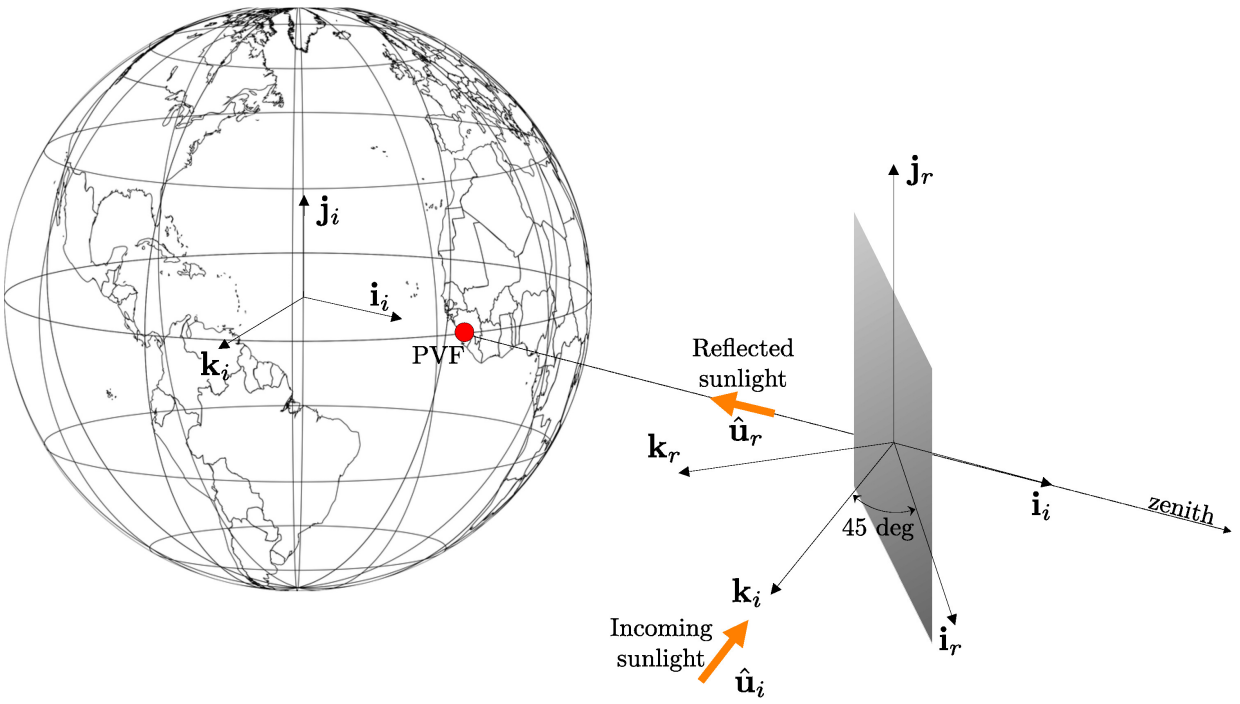

Fig. 3 Reflector at the zenith: conditions for light reflection to a PVF at the Earth's equator.

to an ultra-lightweight structure, made of a 3D-printed polymer or composite material and overlaid with a thin film. This value is also typical for large solar sails. [16]. Now define a reflector-centered reference frame $(xyz)_r$ with axes parallel to the principal directions of inertia of the reflector and unit vectors $\hat{\mathbf{i}}_r$, $\hat{\mathbf{j}}_r$ and $\hat{\mathbf{k}}_r$, where x and y are the in-plane directions and z is the out-of-plane direction. Then, define an inertial reference frame $(xyz)_i$ with unit vectors $\hat{\mathbf{i}}_i$, $\hat{\mathbf{j}}_i$ and $\hat{\mathbf{k}}_i$ in the x_i, y_i and z_i directions, such that $\hat{\mathbf{j}}_i$ is parallel to the Earth's spin axis and $\hat{\mathbf{k}}_i$ is normal to the orbital plane (see Fig. 3). For simplicity, the rotation of the Earth during a reflector pass is neglected, such that the PVF is inertially fixed. This is a reasonable approximation for the orbit altitudes considered in this paper. For example, for a 1000 km (3000 km) altitude, the pass duration is approximately 18 minutes (39 minutes), corresponding to a 4 deg (9.8 deg) rotation of the Earth, or a 3.8 deg (4.56 deg) East-West rotation of the reflector, which can be reasonably neglected. Also, the effect of the Earth rotation around the Sun are neglected.

Let θ be the orbit angle of the reflector, with $\theta = 0$ when the reflector is located at the zenith of the PVF, as shown in Fig. 2. Also, let ϵ be the zenith angle of the reflector such that $\epsilon = 0$ at the zenith. The zenith angle can then be written as a function of the orbit angle as

$$\epsilon = \arcsin\left(\frac{R_o}{d}\sin\theta\right) \tag{1}$$

where d is the distance between the PVF and the reflector such that

$$d = \sqrt{R_E^2 + R_o^2 - 2R_E R_o \cos\theta} \tag{2}$$

Upon simplification, the first and second derivatives of the zenith angle with respect to time can then be written as:

$$\dot{\epsilon} = \frac{R_o\omega_o\left[2(R_o^2 + R_E^2)\cos\theta - R_o R_E(3 + \cos 2\theta)\right]}{2d^2(R_E - R_o\cos\theta)} \tag{3a}$$

$$\ddot{\epsilon} = \frac{R_o\omega_o^2 R_E(R_o^2 - R_E^2)(R_E - R_o\cos\theta)\sin\theta}{2d^4(R_E - R_o\cos\theta)} \tag{3b}$$

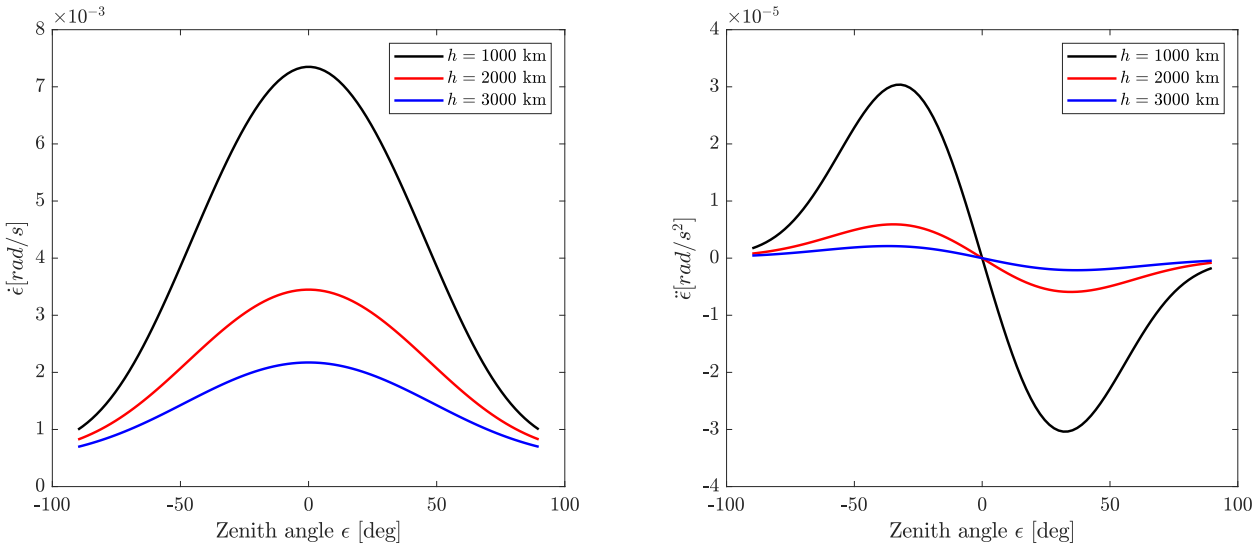

Fig. 4 First and second derivative of the elevation angle as a function of the zenith angle, for a range of orbit altitudes.

where

$$\dot{\theta} = \omega_o = \sqrt{\frac{\mu}{R_o^3}} \tag{4}$$

is the constant orbit angular velocity and $\mu = 3.986 \times 10^{14}$ m^3 s^{-2} is the Earth's gravitational parameter. Figure 4 shows the variation of $\dot{\epsilon}$ and $\ddot{\epsilon}$ as a function of ϵ and the orbit altitude h. The first derivative of the zenith angle has its peak at the zenith, whereas the peak of the second derivative changes depending on the reflector altitude.

III. Control modes, required angular accelerations and disturbances

Two main operation modes can be defined: tracking and reorientation. During tracking the reflector must be steered to continuously reflect sunlight to the PVF, while $-\epsilon_{max} \leq \epsilon \leq \epsilon_{max}$. The parameter $\epsilon_{max} = \max(\epsilon)$ is the maximum zenith angle during the tracking phase. If $\epsilon_{max} = \pi/2$ sunlight is reflected during the entire transit of the reflector above the local horizon. This condition ensures that the maximum amount of energy is delivered to the PVF. Outside the tracking window the reflector must be reoriented to track the next PVF. The peak angular accelerations in these two phases are now discussed and then compared with the orbit perturbations due to gravity gradient, solar radiation pressure and atmospheric drag. In both cases, it is assumed that $\epsilon_{max} = \pi/2$.

A. Tracking

In order to reflect sunlight to the PVF two conditions must be verified. Firstly, the reflector must be tilted at 45 deg with respect to the orbital plane. Secondly the instantaneous axis of rotation must be parallel to $\hat{\mathbf{k}}_i$ such that, at the zenith, the unit vectors $\hat{\mathbf{i}}_i$, $\hat{\mathbf{k}}_i$, $\hat{\mathbf{i}}_r$ and $\hat{\mathbf{k}}_r$ are coplanar, as shown in Fig. 3. Let γ be the reflector rotation angle about $\hat{\mathbf{k}}_i$, such that $\gamma = 0$ when $\epsilon = 0$. Both conditions are satisfied if the reflector rotates about $\hat{\mathbf{k}}_i$ by $\gamma = \epsilon$, starting from the nominal configuration shown in Fig. 3. Thus the reflector angular velocity and angular acceleration during the tracking phase can be written as

$$\boldsymbol{\omega_t} = \dot{\gamma}\hat{\mathbf{k}}_i = \dot{\epsilon}\hat{\mathbf{k}}_i \tag{5a}$$

$$\dot{\boldsymbol{\omega}}_t = \ddot{\gamma}\hat{\mathbf{k}}_i = \ddot{\epsilon}\hat{\mathbf{k}}_i \tag{5b}$$

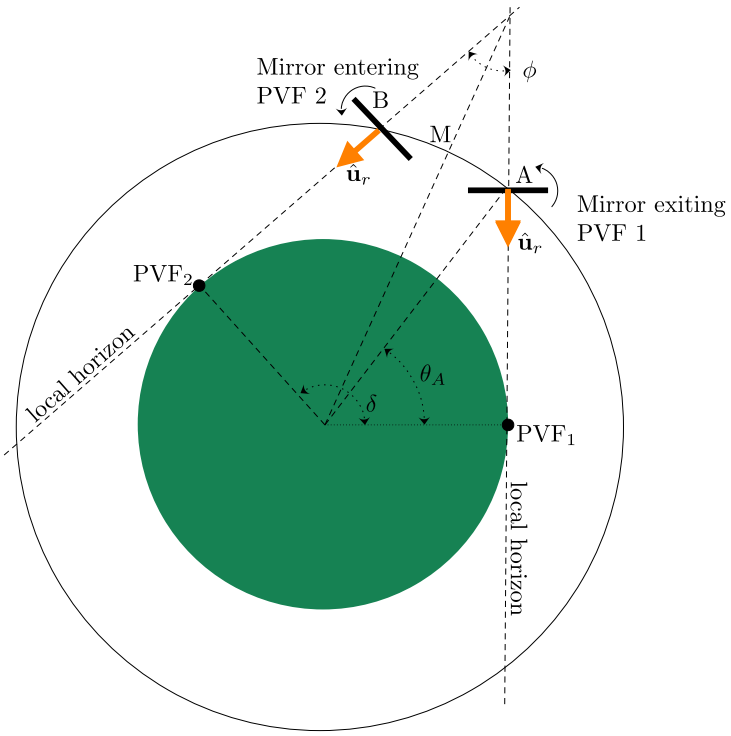

Fig. 5 Orientation of the reflector at endpoints of a reorientation manoeuvre between two adjacent PVFs.

where the derivative of the zenith angle is given by Eq. (3a). Hence, the reflector angular velocity changes at the same rate as the derivative of the zenith angle. The unit vector $\hat{\mathbf{k}}_i$ can be expressed as:

$$\hat{\mathbf{k}}_i = \hat{\mathbf{i}}_r \cos\frac{\pi}{4} + \hat{\mathbf{k}}_r \cos\frac{\pi}{4} \tag{6}$$

Note that Eq. (6) holds true for any zenith angle ϵ when the two conditions defined above are verified. Substituting Eq. (6) into Eqs. (5) yields:

$$\boldsymbol{\omega_t} = \frac{\sqrt{2}}{2}\dot{\epsilon}(\hat{\mathbf{i}}_r + \hat{\mathbf{k}}_r) \tag{7a}$$

$$\dot{\boldsymbol{\omega}}_t = \frac{\sqrt{2}}{2}\ddot{\epsilon}(\hat{\mathbf{i}}_r + \hat{\mathbf{k}}_r) \tag{7b}$$

Note that such angular acceleration can be obtained by providing torques along the reflector axes x_r and z_r. However, since the rotation axis is not a principal axis, additional torque on the y axis should be provided to counteract the induced precession.

B. Reorientation

The reflector reorientation between two consecutive PVFs can be performed by keeping the same rotation axis and angular velocity direction as in the tracking phase, such that the reflector is always inclined by 45 deg with respect to the orbital plane. This has the advantage that no sunlight is reflected to Earth during the reorientation manoeuver (note that this is true only if $\epsilon_{max} = \pi/2$, as in this case). In fact, at the end of the tracking phase, the reflected sunlight beam is tangent to Earth and steered away from the ground. Similarly, at the beginning of a new tracking phase, the reflected sunlight beam is tangent to the PVF when it crosses its local horizon.

Let n_{PVF} be the total number of PVFs to be tracked during one orbit and assume that the difference between their latitude is constant and equal to $\delta = 2\pi/n_{\text{PVF}}$. Now, as represented in Fig. 5, let A and B be the start and end point of

the reorientation maneuver between two adjacent tracking sections, respectively (corresponding to the end of the first PVF tracking and the beginning of the second PVF tracking) and let θ_A, θ_B be the corresponding orbit angles. For simplicity let PVF_1 and PVF_2 indicate two adjacent PVFs to be tracked. To avoid intersection between two consecutive tracking sections, the following constraint holds

$$\Delta\theta_{AB} = \theta_B - \theta_A > 0 \tag{8}$$

which can be written as a function of the latitudinal PVF displacement:

$$\delta - 2\theta_A > 0 \tag{9}$$

Equation (9) defines the minimum angular displacement between the PVFs. If $\delta = 2\theta_A$ the the points A and B are coinciding and the reorientation time would be zero, implying that the required control torque diverges (as $\dot{\omega}_r \to \infty$). The constraint given by Eq. (9) also implies the existence of an upper bound on the number of PVFs that can be visited per orbit, which will be discussed later.

Now, let ϕ be the angle between the reflector normals $\hat{\mathbf{k}}_r$ at the points A and B (see Fig.5). Using elementary geometry, the angle ϕ can be written as a function of ϵ and δ such that $\phi = |2\epsilon - \delta|$. It is apparent from Fig. 5 that the required reflector rotation is (assuming only one reflective side) $\Delta\gamma_{AB} = \gamma_B - \gamma_A = 2\left(\pi - \frac{\phi}{2}\right) + 2k\pi$ plus an arbitrary integer number of complete rotations $2k\pi$, where $k \in \mathbb{N}$. If both sides of the reflector are covered by reflective membranes then the required rotation is smaller and equal to: $\Delta\gamma_{AB} = 2\left(\frac{\pi}{2} - \frac{\phi}{2}\right) + 2k\pi$. Hence the required reflector rotation for a single-sided reflector (SSR) and double-sided reflector (DSR) is:

$$\Delta\gamma_{AB} = \begin{cases} 2\left(\pi - \frac{\phi}{2}\right) + 2k\pi = 2(1+k)\pi - \phi, & \text{SSR} \\ 2\left(\frac{\pi}{2} - \frac{\phi}{2}\right) + 2k\pi = (1+k)\pi - \phi, & \text{DSR} \end{cases} \tag{10}$$

Assuming a bang-bang reorientation manoeuver, the angular acceleration $\dot{\omega}_r$ follows from:

$$\frac{\Delta\gamma_{AB}}{2} = \omega_A \Delta t_{AM} + \frac{1}{2}\dot{\boldsymbol{\omega}}_r (\Delta t_{AM})^2 \tag{11}$$

such that

$$\dot{\omega}_r = \frac{\Delta\gamma_{AB} - 2\omega_A \Delta t_{AM}}{(\Delta t_{AM})^2} \tag{12}$$

where ω_A is the residual angular acceleration of the reflector at point A (note that this is also the angular velocity of the reflector at point B) and $(\Delta t)_{AM}$ is the orbital time associated to the arc AM, i.e.,

$$\Delta t_{AM} = \frac{\theta_M - \theta_A}{\omega_o} \tag{13}$$

Figure 6 shows the orientation of the reflector at the endpoints (A and B) and midpoint (M) of the reorientation manoeuver for a SSR and DSR.

The angular acceleration clearly changes as a function of the integer k (Eq. (10)). It is reasonable to choose k such that the reorientation angular acceleration $\dot{\omega}_r$ is minimum (to minimize the required torque), i.e.,:

$$k = \arg\min_{k \in \mathbb{N}} |\dot{\omega}_r| \tag{14}$$

Substituting Eqs. (10) and (13) into Eq. (12), the required reorientation acceleration can be found as a function of the orbit altitude, the tracking angle and the number of PVFs to be tracked. If $\dot{\omega}_r > 0$ then the reflector is accelerated during the reorientation phase and the maximum angular velocity may exceed the maximum angular velocity during the tracking phase. In this case, the actuator will need to provide more angular momentum during the reorientation maneuver. Conversely, if $\dot{\omega}_r < 0$, the reflector is decelerated during the reorientation. Then:

$$\begin{cases} \max(\omega_r) = \omega_A, & \text{if } \dot{\omega}_r < 0 \\ \max(\omega_r) = \omega_A + |\dot{\omega}_r|\Delta t, & \text{if } \dot{\omega}_r > 0 \end{cases} \tag{15}$$

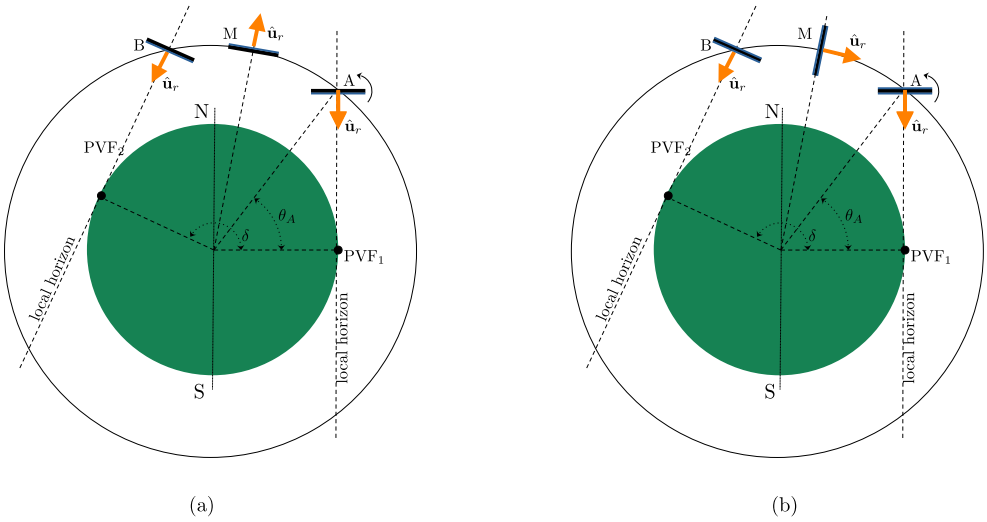

Fig. 6 Reflector orientation at endpoints and midpoint, in case of single-sided reflector (a) and double sided reflector (b). The reflector is here represented as a segment perpendicular to the reflected light direction. The light is coming from outside the page.

Figure 7 shows the angular velocity and angular acceleration during the reorientation phase as a function of the orbit altitude and of n_{PVF}, compared with the peak tracking angular velocity and angular acceleration, represented as a dashed black line, for a SSR. For a given n_{PVF} the reorientation angular velocity and angular acceleration is below the corresponding tracking values below a certain maximum altitude. Note that, for $n_{\text{PVF}} = 4$, the maximum azimuth angle must be reduced below $\pi/2$ above a certain altitude to ensure that condtion (9) is verified. This explains the non-continuity of the first derivatives of the curves in Fig. 7 for $n_{\text{PVF}} = 4$.

The green line in Fig. 8 shows the maximum number of PVFs that can can be tracked per orbit as a function of the orbit altitude and verify $\omega_r < \max(\omega_t)$ and $\dot{\omega}_r < \max(\dot{\omega}_t)$, for a SSR (a) and a DSR (b). Also shown with a orange line is the maximum number of PVFs that can be tracked ensuring that consecutive tracking regions do not intersect (Eq. (8)). For example, at an altitude of 1000 km and taking a SSR, up to 5 PVFs can be tracked. If $1 \leq n_{\text{PVF}} \leq 3$, the angular velocity and angular acceleration during the reorientation phase do not exceed the corresponding peak values during the tracking phase. Conversely, for $4 \leq n_{\text{PVF}} \leq 5$ the actuator should be designed based on the requirements on the reorientation phase. The required angular acceleration is smaller for a DSR and therefore, at the same orbit altitude, the tracking angular velocity and angular acceleration are dominant up to 4 PVFs, rather than 3. It is interesting to observe that above 6371 km only two PVFs can be tracked per orbit. However, such altitude threshold is reduced to 1290 km (or 1880 km for a DSR) to ensure that $\omega_r < \max(\omega_t)$ and $\dot{\omega}_r < \max(\dot{\omega}_t)$.

In the following section, the angular accelerations during the tracking and reorientation phase are compared with other torque disturbances.

C. Comparison with disturbances

The main disturbances include perturbations due to gravity gradient, solar radiation pressure and atmospheric drag. The maximum gravity gradient torque occurs when the structure is pitched at a 45 deg angle to the local vertical. Under these conditions it is found that [17]

$$T_{grav} = \frac{\mu \rho_r l^4}{8 R_o^3} \tag{16}$$

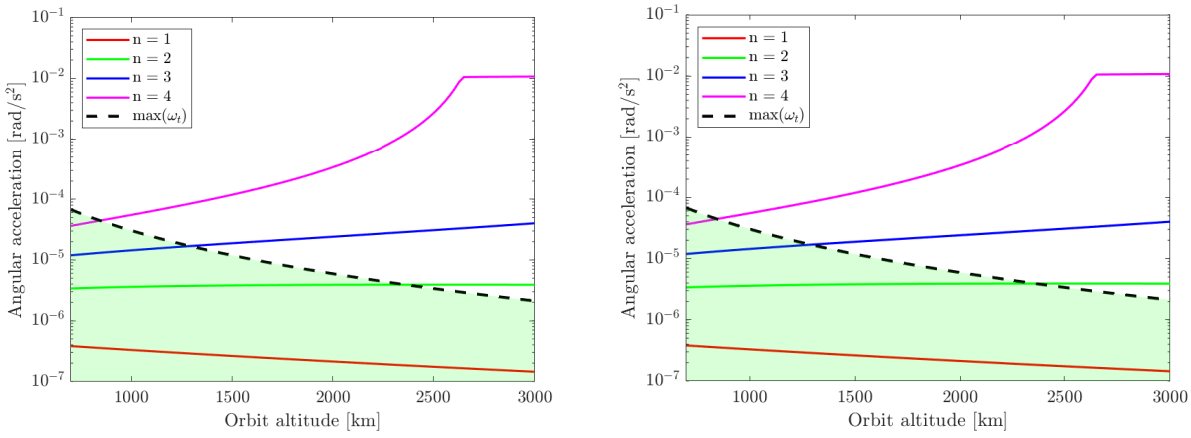

Fig. 7 Angular velocity and angular acceleration during reorientation and tracking phase, as a function of the orbit altitude and of the number of PVFs per orbit.

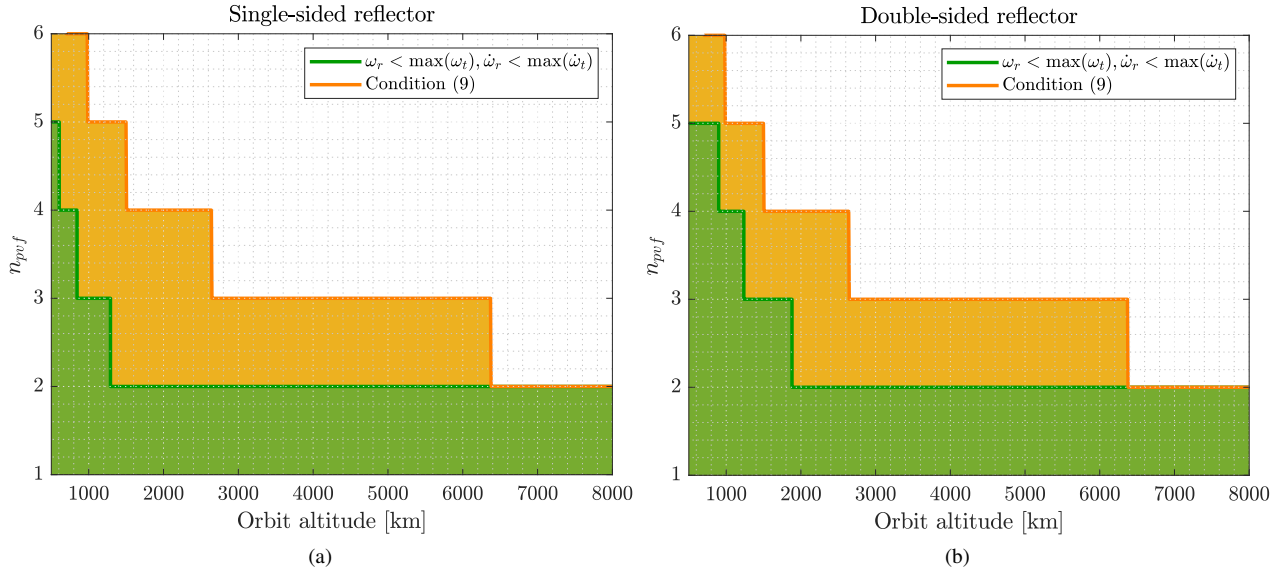

Fig. 8 Maximum number of PVFs that can be tracked during one orbit such that the angular velocity and angular acceleration during the reorientation phase are smaller than the tracking phase (green line) and such that adjacent tracking sections do not intersect (orange line), for a single-sided reflector (a) and a double-sided reflector (b).

then, dividing by the reflector in-plane inertia $\rho_r l^4/12$ yields the equivalent angular acceleration, which is independent of the reflector size and only scales with the cube of the orbit radius *:

$$\dot{\omega}_{grav} = \frac{3}{2}\frac{\mu}{R_o^3} \tag{17}$$

Furthermore, assuming perfect reflector reflectivity, the SRP torque can be written as

$$T_{srp} = (2p_{srp}l^2\cos^2\beta)\delta_{srp} \tag{18}$$

where the terms inside the brackets is the SRP force acting on the reflector [20], $p_{srp} = 4.56 \times 10^{-6}\,\mathrm{N\,m^{-2}}$ is the solar radiation pressure, β is the angle between the reflector normal and the light direction and δ_{srp} is the offset between the center-of-pressure (CoP) and center-of-mass (CoM) of the reflector. Assuming δ_{srp} scales as $2.5 \times 10^{-2} l$ [20], setting $\beta = 45$ deg and dividing the torque by the in-plane reflector inertia yields:

$$\dot{\omega}_{srp} = 3 \times 10^{-1}\frac{p_{srp}}{\rho_r l} \tag{19}$$

hence the SRP-induce angular acceleration is smaller for larger structures.

Lastly, the aerodynamic drag torque can be written as

$$T_{drag} = \left(\frac{1}{2}\rho_{atm}C_d l^2 v^2\right)\delta_{drag} \tag{20}$$

where the term inside the brackets is the resistance force due to drag [22], ρ_{atm} is the density of the atmosphere, C_d is the aerodynamic drag coefficient, v is the reflector orbital velocity and δ_{drag} is the offset between the reflector center-of-aerodynamic pressure and the CoM. For a flat plate $C_d \approx 2.2$ [23] and the atmosphere density is modeled using a simple exponential model [24] From Ref. [25], δ_{drag} is approximately 0.2 m for a 100 m solar sail at an altitude of 400 km. It is then assumed for simplicity that δ_{drag} scales as $2 \times 10^{-3} l$. Then, dividing the torque by the in-plane reflector inertia and simplifying, the equivalent atmospheric drag-induced angular acceleration can be found as:

$$\dot{\omega}_{drag} = 2.6 \times 10^{-2}\frac{\rho_{atm}v^2}{\rho_r l} \tag{21}$$

Figure 9 compares the equivalent angular acceleration due to external perturbations with the peak tracking and reorientation accelerations. The reorientation accelerations are shown in the case of tracking two equidistant PVFs. It is apparent that below 3000 km the tracking angular acceleration is dominant in case of a DSR. If a SSR reflector is used then the reorientation angular acceleration is larger for altitudes above approximately 2300 km. The SRP-induced acceleration and the atmospheric drag acceleration are overall negligible for the altitude range considered here.

IV. Comparison of attitude control actuators

The attitude control actuator must be designed in order to deliver the peak torque required in the worse-case scenario. The torque is proportional to the angular acceleration (which depends on the reflector orbit, as discussed in the previous section) and the reflector inertia. If the areal density of the reflector is constant, then the required torque scales as l^4, suggesting that the required torques rapidly increase for large structures. In this section the performances of different actuators will be discussed, in terms of their mass and power requirements. It is assumed that a DSR is employed to track two equidistant PVFs per orbit and a range of altitudes between 1000 km and 3000 km is considered. Under these assumptions and following the results in the previous section, the tracking angular acceleration can be used as a design parameter to derive the required torques and therefore actuator mass. Higher altitudes will likely be of less interest for this application, since the power density of the reflected light significantly decays at higher orbital radius [26]. Furthermore, in order to simplify the comparison of different families of actuators, it is assumed that the manoeuver is about one of the reflector in-plane axes, with a reference angular acceleration given by the absolute value of the tracking angular acceleration (Eq. (7b)), i.e., $\dot{\omega} = \ddot{\epsilon}$. This neglects the full 3 axis control problem (which is outside the scope of

*For consistency, the angular acceleration is indicated using the same symbol as in Eq. (5) and the same convention is used for the other perturbations discussed. However, it must be noted that the direction of the angular acceleration vector will in general be different from Eq. (5)

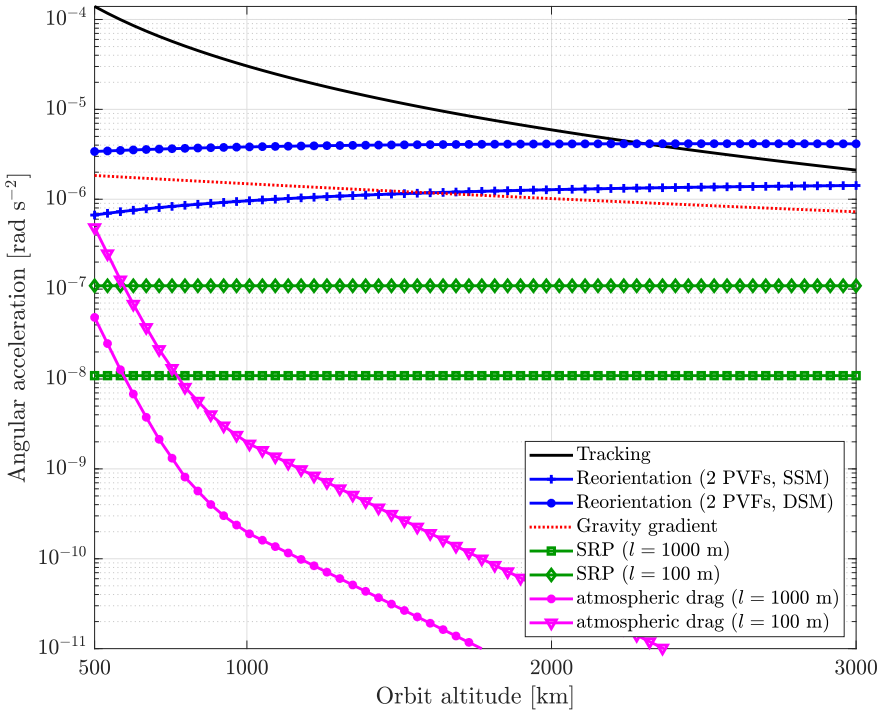

Fig. 9 Maneuver peak angular acceleration due to tracking and reorientation of the reflector and equivalent angular acceleration caused by disturbances as a function of the orbit altitude.

this paper) while providing key information about advantages and disadvantages of each actuator for such applications.

The actuators considered are: control moment gyro (CMG), reaction wheel (RW), methods based on SRP, current loops and thrusters.

A. Control Moment Gyro

In its simplest form, a CMG is a spinning fly-wheel mounted on a gimbal. By rotating the gimbal, the wheel angular momentum vector is rotated thus generating a torque. In general, various CMG architectures can be used, including, for example, pyramidal CMG structures or gimbals with multiple degrees of freedom [20]. Here, for simplicity, a pair of counter-rotating CMGs is chosen with a disk shape, radius R_w and thickness t (see Fig. 10a). The counter-rotating configuration has the main advantage of minimizing cross-coupling between control axes [27]. The wheels are nominally spinning in opposite directions with constant angular velocity ω_w and they can be gimballed with respect to y_r by applying a torque T_m. Let ϕ be the gimbal angle (with $\phi = 0$ when the wheels are parallel to the xy plane). It is desirable to keep the gimbal angle below a threshold value, to avoid saturation [27] and interference between the wheel and the reflector. Here, following Ref. [10], a reference value of $\phi_{max} = 10\,\text{deg}$ is taken.

Let $\mathbf{H}_{w1}$ and $\mathbf{H}_{w2}$ be the angular momenta of the first and second wheel. In the reflector body frame, the wheel angular momenta can be expressed as:

$$\mathbf{H}_{w1} = \begin{Bmatrix} I_w\omega_w \sin\phi \\ (I_w/2)\dot{\phi} \\ I_w\omega_w \cos\phi \end{Bmatrix}, \quad \mathbf{H}_{w2} = \begin{Bmatrix} I_w\omega_w \sin\phi \\ -(I_w/2)\dot{\phi} \\ -I_w\omega_w \cos\phi \end{Bmatrix} \tag{22}$$

where the y_r components of the angular momentum vector are caused by the rotation of the wheel about the gimbal axis

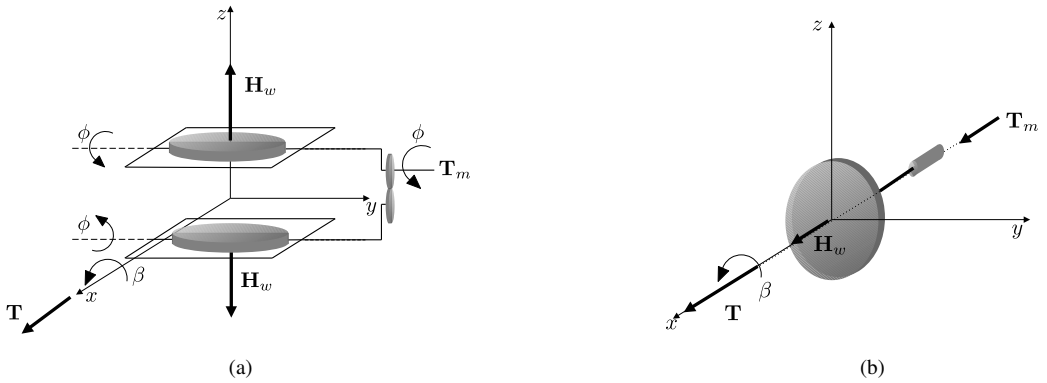

Fig. 10 (a): Double 1-DOF control moment gyro. (b): Reaction wheel.

and

$$I_w = \frac{1}{2} m_w R_w^2 \tag{23}$$

$$I_r = \frac{1}{6} m_r l^2 \tag{24}$$

are the inertia of the wheel with respect to its spin axis and the inertia of the reflector with respect to its normal respectively.

The reaction torques $\mathbf{T}_1$ and $\mathbf{T}_2$ generated by the two wheels on the reflector are therefore given by:

$$\mathbf{T}_i = -\frac{d}{dt}\mathbf{H}_i = -\left(\frac{\partial}{\partial t}\mathbf{H}_i + \boldsymbol{\omega} \times \mathbf{H}_i\right) \quad i = 1, 2 \tag{25}$$

Upon simplifications, Eq. (25) can be used to define the total torque $\mathbf{T}$ as:

$$\mathbf{T} = -2 I_w \omega_w \left(\dot{\phi} \cos\phi \, \hat{\mathbf{i}}_r + \omega_z \sin\phi \, \hat{\mathbf{j}}_r - \omega_y \sin\phi \, \hat{\mathbf{k}}_r\right) \tag{26}$$

Therefore, neglecting external perturbations, the Euler equations describing the reflector dynamics can be written as:

$$\begin{cases} I_x \dot{\omega}_x + (I_z - I_y)\omega_y \omega_z &= -2 I_w \omega_w \dot{\phi} \cos\phi \\ I_y \dot{\omega}_y + (I_x - I_z)\omega_z \omega_x &= -2 I_w \omega_w \omega_z \sin\phi \\ I_z \dot{\omega}_z + (I_y - I_x)\omega_y \omega_x &= 2 I_w \omega_w \omega_y \sin\phi \end{cases} \tag{27}$$

Here, the terms I_x, I_y, I_z represent the inertia of the reflector and wheels. Due to the gimbal rotation, the wheel inertia is time-dependent and therefore I_x, I_y, I_z are not constant. However, given that the maximum gimbal angle ϕ_{max} is small, it is reasonable to assume the wheels are parallel to the xy plane during the entire duration of the maneuver. It follows that:

$$\begin{cases} I_x = I_r/2 + 2(I_w/2) + 2 m_w \Delta z^2 \\ I_y = I_r/2 + 2(I_w/2) + 2 m_w \Delta z^2 \\ I_z = I_r + 2 I_w \end{cases} \tag{28}$$

where Δz is the distance between the CoM of the wheel and the CoM of the reflector. Assuming $\Delta z \ll l$, then

$$I_x = I_y \approx I_r/2 + I_w \tag{29}$$

Since $I_x = I_y$ for a symmetric reflector and the gimbal angle is small, it follows from Eqs. (27) that the dynamics is restricted to the x-axis with $\boldsymbol{\omega} \approx \{\omega_x, 0, 0\} = \{\dot{\beta}, 0, 0\}$, where β indicates the rotation angle with respect to the x_r axis.

Then

$$I_x|\ddot{\beta}_x| \approx 2I_w\omega_w|\dot{\phi}| \tag{30}$$

where the absolute values of the angular acceleration $\ddot{\beta}$ and angular velocity $\dot{\phi}$ have been considered since their sign is not relevant in the following analysis. Then, integrating both sides of Eq. (30) with respect to time yields

$$I_x|\Delta\dot{\beta}| = 2I_w\omega_w|\Delta\phi| \tag{31}$$

where $\Delta\dot{\beta}$ is the variation of the reflector angular velocity corresponding to a given rotation $\Delta\phi$ of the gimbal. The required wheel inertia can now be found by imposing $|\dot{\phi}| < \dot{\phi}_{max}$ and $|\Delta\phi| < \phi_{max}$, where $\dot{\phi}_{max}$ is the maximum gimbal rate. Here, for simplicity, it is assumed $\dot{\phi}_{max}$ is a free parameter and only the constraint on the saturation angle holds. [†] Then, setting $\Delta\phi = \phi_{max}$ when $\Delta\dot{\beta} = \Delta\dot{\beta}_{max}$, the required wheel inertia can be calculated, using the saturation avoidance constraint as:

$$I_w = \frac{I_r}{2}\frac{\Delta\dot{\beta}_{max}}{2\omega_w\phi_{max} - \dot{\beta}_{max}} \tag{32}$$

The value $\Delta\dot{\beta}_{max}$ represents the maximum variation of the angular velocity during the tracking phase and can be calculated via Eq. (3a). For a 1000 km orbit $\Delta\dot{\beta}_{max} \approx 7 \times 10^{-3}\,\mathrm{rad\,s^{-1}}$. From now, the symbol Δ will be omitted to simplify the notation.

Then, given the wheel inertia, the total mass of the two CMGs $2m_w$ can be written as:

$$2m_w = \frac{1}{6}\frac{\dot{\beta}_{max}}{2\omega_w\phi_{max} - \dot{\beta}_{max}}\frac{\rho_r l^4}{R_w^2} \tag{33}$$

In principle, by increasing the wheel angular velocity, the wheel mass can be reduced. However, ω_w is practically limited by the material strength of the wheel and the type of bearings used. The maximum stress of a rotating disk occurs at its center and depends on the wheel angular velocity via [28]:

$$\sigma_{max} = \frac{3+\nu}{8}\rho_w\omega_w^2 R_w^2 \tag{34}$$

where ν is the Poisson's ratio of the material. Solving Eq. (34) for ω_w, substituting it into Eq. (33) and simplifying yields:

$$2m_w \approx \frac{1}{12}\sqrt{\frac{3+\nu}{8}}\sqrt{\frac{\rho_w}{\sigma_{max}}}\frac{\dot{\beta}_{max}}{\phi_{max}}\frac{\rho_r l^4}{R_w} \tag{35}$$

where the approximation follows from $\dot{\beta}_{max} \ll 2\omega_w\phi_{max}$. Note that this is a reasonable approximation even for hypothetical very large/slow-rotating wheels. For example, $\dot{\beta}_{max}/2\omega_w\phi_{max} < 7 \times 10^{-3}$ for a wheel made of 4340 steel [28] and $R_w \leq 100\,\mathrm{m}$, with $h = 1000\,\mathrm{km}$. For a given reflector side-length, the wheel mass can therefore be reduced using material with a low stress-to-density ratio σ_{max}/ρ_w or by increasing the radius of the wheel.

The motor torque T_m required to drive the gimbal is:

$$T_m = (\mathbf{T}_1 - \mathbf{T}_2)\cdot\hat{\mathbf{j}}_r \tag{36}$$

where the minus sign on $\mathbf{T}_2$ is used since the wheels are gimballed in opposite directions. Substituting Eqs. (25) into Eq. (36) and simplifying yields:

$$T_m = -2I_w\omega_w\dot{\beta}\cos\phi + 2I_w\ddot{\phi} \tag{37}$$

Since the maximum gimbal angle ϕ_{max} is small and neglecting the gimbal acceleration, the motor torque can then be approximated as:

$$T_m \approx -2I_w\omega_w\dot{\beta} \tag{38}$$

Then, the power P required during the manoeuvre is, by definition:

$$P_{max} = |T_m\dot{\phi}| \tag{39}$$

[†] If the wheel mass is much smaller than the reflector mass, the reflector inertia is independent of the wheel inertia, therefore the Eq. (31) could be directly solved with respect to the wheel angular momentum $I_w\omega_w$. However, here a more general case in considered, where the wheel inertia can be large, such that I_x also depends on I_w.

Assuming for simplicity that T_m and $\dot{\phi}$ have a peak at the same time [‡], i.e., substituting $\dot{\beta} = \dot{\beta}_{max}$ and $\dot{\phi} = \dot{\phi}_{max}$ (this is given by Eq. (30) for $\ddot{\beta} = \ddot{\beta}_{max}$), the maximum power can be estimated. Again using the approximation $\dot{\beta}_{max} \ll 2\omega_{w,max}\phi_{max}$ and further simplifying yields:

$$P_{max} \approx \frac{1}{6}\rho_r l^4 \ddot{\beta}_{max}\dot{\beta}_{max} \tag{40}$$

Note that the maximum power scales with l^4 and it is proportional to the peak angular acceleration $\ddot{\beta}_{max}$ and angular velocity $\dot{\beta}_{max}$.

It is interesting to compare the average power with the available input power P_{in} that can be generated via photovoltaic conversion. For a 45 deg angle between the reflector normal and incoming sunlight:

$$P_{in} = \eta_e \eta_A A_r P_\odot \cos\left(\frac{\pi}{4}\right) \tag{41}$$

Here, η_e represents the overall efficiency of the photovoltaic conversion, η_A is the fraction of the reflector area used for photovoltaic conversion, $A_r = l^2$ is the reflector area and $P_\odot = 1327\,\mathrm{W\,m^{-2}}$ is the solar constant. Then the condition $P_{max} < P_{in}$ defines an upper bound on the reflector side l

$$l_{\max} < \sqrt{\frac{6\eta_e \eta_A P_\odot}{\sqrt{2}\rho_r \ddot{\beta}\dot{\beta}_{max}}} \tag{42}$$

B. Reaction wheel

A reaction wheel transfers torque to a body by changing the magnitude of its angular momentum, rather than its direction. Consider a single wheel with spin axis aligned with the reflector x_r axis, as shown in Fig 10b. Its angular momentum $\mathbf{H}$ is given by:

$$\mathbf{H}_w = I_w \omega_w \hat{\mathbf{i}}_r \tag{43}$$

Hence, the resulting torque on the reflector is parallel to the x-axis such that:

$$\mathbf{T} = -\frac{d}{dt}\mathbf{H}_w = -I_w \dot{\omega}_w \hat{\mathbf{i}}_r \tag{44}$$

It follows that:

$$I_x \ddot{\beta} = -I_w \dot{\omega}_w \tag{45}$$

Integrating both sides of Eq. (45) with respect to time yields:

$$I_x |\Delta\dot{\beta}| = I_w |\Delta\omega_w| \tag{46}$$

where $|\Delta\omega_w|$ is the variation of the wheel angular velocity. The wheel reaches its maximum angular velocity $\omega_{w,max}$ when $\dot{\beta}$ is maximum, i.e., $|\Delta\omega_w| = \omega_{w,max}$ and $|\Delta\dot{\beta}| = \dot{\beta}_{max}$. Also, the total inertia of the system wheel and reflector is given by $I_x = I_r/2 + I_w$. Thus, from Eq. (45), the required wheel inertia can be found as:

$$I_w = \frac{I_r}{2}\frac{\dot{\beta}_{max}}{\omega_{w,max} - \dot{\beta}_{max}} \tag{47}$$

Typically, the maximum angular velocity of the wheel is several orders of magnitude larger than the maximum angular velocity required for the manoeuvre, hence:

$$I_w \approx \frac{I_r}{2}\frac{\dot{\beta}_{max}}{\omega_{w,max}} \tag{48}$$

where the approximation follows from $\dot{\beta}_{max} \ll \phi_{max}$. Then, the required wheel mass is given by:

$$m_w = \frac{1}{12}\frac{\rho_r l^4}{R_w^2}\frac{\dot{\beta}_{max}}{\omega_{w,max}} \tag{49}$$

[‡]This is not true in general, however it is a conservative assumption.

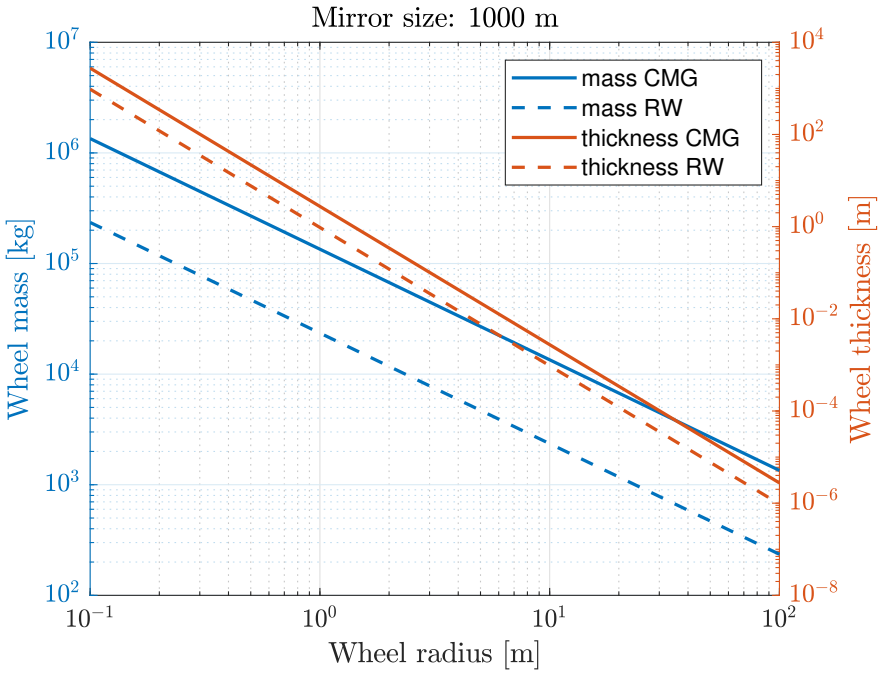

Fig. 11 CMG (continuous line) and RW (dashed line) mass and thickness requirements as a function of the wheel radius, for an orbit altitude $h = 1000\,\mathrm{km}$ and a reflector size $l = 1000\,\mathrm{m}$

As in Sec.IV.A, the wheel angular velocity can be expressed as a function of the material strength. In this case:

$$m_w \approx \frac{1}{12}\sqrt{\frac{3+\nu}{8}}\sqrt{\frac{\rho_w}{\sigma_{max}}}\dot{\beta}_{max}\frac{\rho_r l^4}{R_w} \tag{50}$$

The required motor torque is defined as:

$$T_m = -I_w\dot{\omega}_w \tag{51}$$

Using the same assumption as in the previous section, the maximum power is then:

$$P_{max} = |T_m\omega_w| \approx \frac{1}{12}\rho_r l^4\omega_{w,max}\ddot{\beta}_{max} \tag{52}$$

Contrary to the CMG case, here the average power is proportional to the maximum angular velocity of the wheel rather than the maximum angular velocity of the reflector. As in Section IV.A, an upper bound on the reflector size can be found. In this case:

$$l_{\max} < \sqrt{\frac{12\eta_e\eta_A P_\odot}{\sqrt{2}\rho_r\omega_{w,max}\ddot{\beta}}} \tag{53}$$

C. Results for momentum exchange devices

Figure 11 compares the required CMG and RW mass as a function of the wheel radius, for $l = 1000\,\mathrm{m}$. For reference, the material properties are referred to 4340 steel, with density $\rho_w = 7800\,\mathrm{kg\,m^{-3}}$ and tensile stress 1800 MPa [28]. Here the maximum stress σ_{max} is fixed to 10% of the tensile stress and $\nu = 0.3$. The required wheel mass for the CMG is approximately 5.7 times higher than that of a RW and this factor only depends on the CMG gimbal saturation angle (compare Eqs. (35) and (50)). Therefore, for a given wheel mass, larger CMG wheels are needed compared to RW. For example, the wheel radius should be at least 2.2 m for a RW and 13.5 m for a CMG to satisfy the requirement $m_w \leq m_r$. Figure 12 shows the mass ratio m_w/m_r as a function of the wheel radius and the reflector size at an altitude of 1000 km new figure (a) and 3000 km (b), taking steel as wheel material. As expected, the ratio increases significantly at larger reflector size and smaller wheel size. The CMG mass can be decreased by allowing larger gimbal angles although this

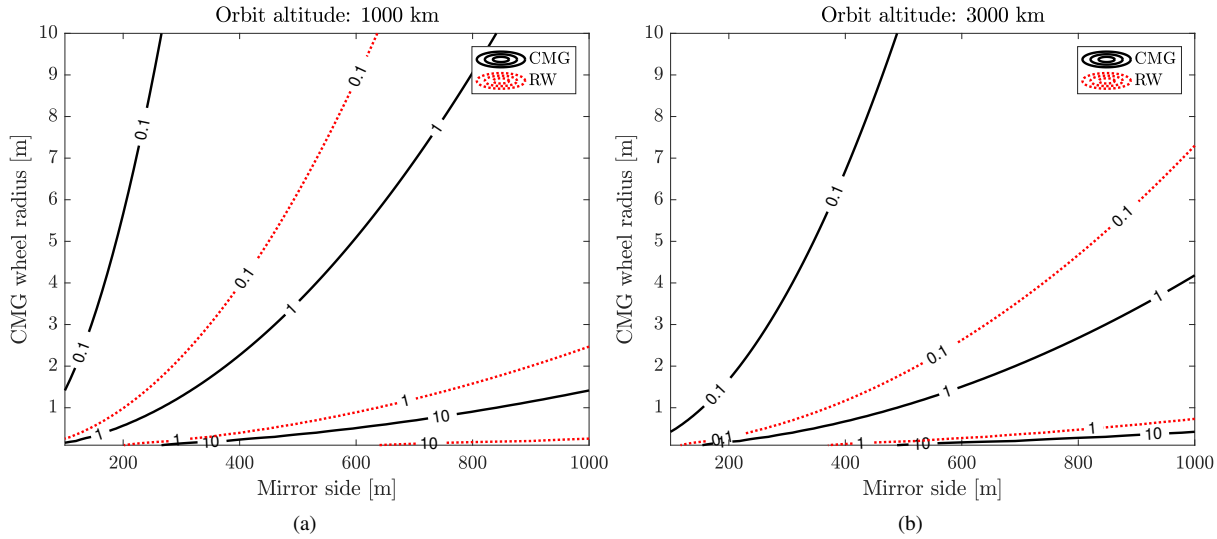

Fig. 12 Mass ratio m_w/m_r as a function of the orbit altitude and the wheel radius, for an altitude of 1000 km (1) and 3000 km (b)

will lead to saturation issues, as discussed. Also shown in Fig. 11 is the required wheel thickness. Clearly, smaller wheels must be thicker due to the larger mass required and the wheel shape will become an oblate cylinder for $R_w < 1$ m.

By inspection of Eqs. (35) and (50), the wheel mass is proportional to the square root of the material specific strength (σ_{max}/ρ_w). Speculatively, a wheel made of graphene (with strength up to 130 GPa [29] and density 2267 kg m^{-3} [§]), has a specific strength 248 times larger than 4340 steel, thus the mass requirements can be reduced by a factor $\sqrt{248} \approx 16$ and allowing smaller wheels to be used. In this case, the constraint $m_w \leq m_r$ is verified for $R_w > 0.1$ m for a RW and $R_w > 0.8$ m for a CMG. Yet, in order to significantly reduce the mass, the wheel radius should be on the order of 10 meters. For example, a pair of 20-meter diameter graphene CMGs would have a total mass of only 400 kg per wheel with a thickness of approximately 0.5 mm.

Due to the l^4 inertia scaling, the requirements for smaller reflector are significantly reduced. For example, the mass requirements for a 100-meter reflector are reduced by a factor 10^4. Thus, a 25-centimeter CMG with total mass of 50 kg would suffice for the tracking requirements of a 100 m reflector on a 1000 km orbit.

By comparing Eqs. (40) and (52) the power requirements for a CMG are significantly smaller. In fact, the CMG motor transfers the torque to the gimbal, whereas the RW transfers torque to the wheel, which is spinning at a much larger rate than the gimbal. For example, a pair of CMGs with $R_w = 10$ m on a 1000 m reflector require 372 W, whereas a RW would require 0.6 MW.

Using the available power criterion, an upper bound on the reflector size was found via Eqs. (42) and (53) for the CMG and RW respectively. Assuming $\eta_e = 0.2$ and $\eta_A = 0.2$ such upper bounds are 3.2×10^5 m and 7.7×10^3 m for the CMG and RW respectively (taking $R_w = 10$ m). The very large value found for the CMG suggests that due to the very low power requirements, enough power can be generated to control an arbitrarily large reflector. Clearly other issues not considered in this analysis, e.g., due reflector flexibility and vibration, will inevitably further limit the maximum reflector size.

It is instructive to evaluate the CMG upper limit considering existing technology for attitude control of large structures, e.g., the CMGs mounted on the International Space Station (ISS). A single ISS CMG generates a nominal angular momentum $H_w = 4760$ N m [30]. Then, for a pair of such CMG, from Eq. (31) it follows that the maximum reflector dimension allowed is approximately 150 m for a 1000 km orbit or 173 m for orders of magnitude smaller than the power-based upper bound, suggesting that improvements in CMG technologies are required to control larger reflectors.

[§] `https://www.quantachrome.com/general_pdf/graphene.pdf`, accessed on 26 August 2021

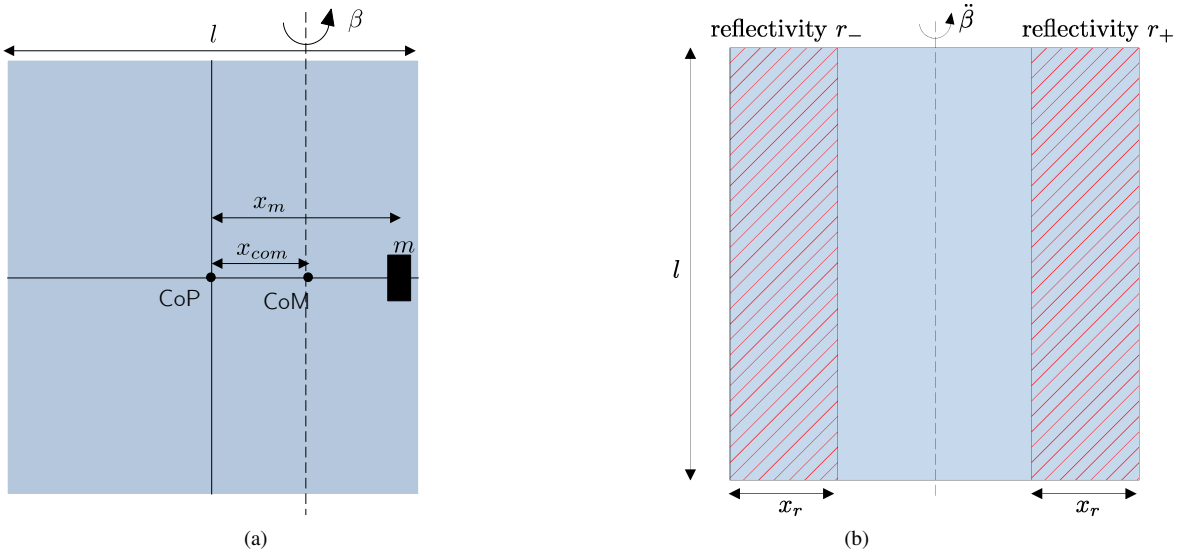

Fig. 13 SRP-based attitude control methods. (a) reflector with a sliding mass that changes the location of the center-of-mass. (b) Variable reflectivity reflector.

D. Sliding masses

The attitude of the reflector can be changed by exploiting SRP. The force caused by the SRP acting at CoP of the reflector (which coincides with its geometric center if the reflectivity is uniform and the reflector is perfectly flat) generates a torque with respect to CoM of the reflector. By actively changing the location of the CoM, for example using sliding masses on the surface of the reflector, the magnitude of such a torque can be modified. Usually, this method is used for small adjustments of solar sails due to external perturbations [20]. Here, the possibility of extending this method for larger maneuvers is explored, using the reference angular acceleration of the reflector for a range of orbit altitudes.

Assume for simplicity that a single mass m_s can slide without friction on a rail positioned along the reflector's y_r axis, such that the resulting torque is parallel to the x_r-axis, where the axes are defined in Section II. Let x_m be the position of the sliding mass with respect to the CoP. The distance between the geometric center of the reflector and the CoM of the system reflector and sliding mass is therefore:

$$x_{com} = \frac{m_s x_m}{m_r + m_s} \tag{54}$$

Then, assuming a perfectly reflective reflector, the magnitude of the torque caused by the SRP is given by [20]:

$$T = 2 p_{srp} A_r x_{com} \cos^2 \beta \tag{55}$$

where the sunlight is assumed to be normal to the reflector when $\beta = 0$. Note that the reflector does not rotate about its geometric center but about the CoM. The angular momentum of the system reflector and sliding mass is therefore

$$H = \left[\frac{I_b}{2} + m_r x_{com}^2 + m_s (x_m - x_{com})^2 \right] \dot{\beta} \tag{56}$$

where the term inside the square brackets is the total inertia of the system, being the sum of the reflector inertia and the sliding mass inertia. Upon simplification, the equation $T = dH/dt$ governing the reflector rotation becomes:

$$\ddot{\beta} = \frac{12(m_s/m_r) x_m \left(p_{srp} \cos^2 \beta - \rho_r \dot{\beta} \dot{x}_m \right)}{\rho_r \left[l^2 + (l^2 + 6x_m^2) m_s/m_r \right]} \tag{57}$$

It is worth noting that a positive sliding mass velocity $\dot{x}_m > 0$ counteracts the positive torque caused by the solar

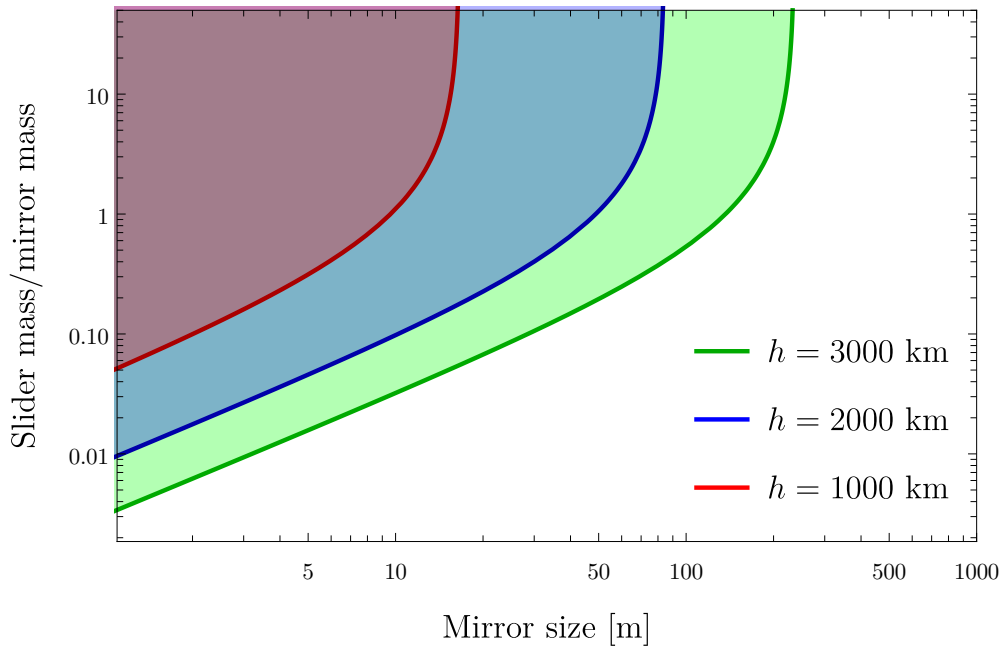

Fig. 14 Slider mass ratio m_s/m_r as a function of the reflector mass.

radiation pressure if the reflector is rotating with non-zero angular velocity, thus decreasing the angular acceleration $\ddot{\beta}$. This is due to the Coriolis-induced torque generated by the sliding mass which is opposite to the SRP torque if the sliding mass is moving towards the edge of the reflector. Conversely, when the sliding mass is moving towards the center of the reflector ($\dot{x}_m < 0$), the resulting Coriolis-induced torque has the same direction as the SRP torque. Eventually, Eq. (57) can be solved for m_s to estimate the minimum mass for a given acceleration profile $\ddot{\beta}$. Here, a set of simplifying assumptions is made to avoid solving the equation of motion directly and to obtain an estimate of the required sliding mass m_s using average values for the reflector angle and the sliding mass position. In particular, assuming that the reflector is pitched at 45 deg with respect to the sunlight and that the sliding mass is located halfway between the CoP and the reflector edge (i.e., $x_m = l/4$), then:

$$m_s = \frac{8 m_r \rho_r \ddot{\beta}}{12 p_{srp} - 24 \rho_r \dot{x}_m \dot{\beta} - 11 l \rho_r \ddot{\beta}} \tag{58}$$

In principle, a "reference" sliding mass velocity $\dot{x}_m$ could be chosen such that the slider can reach the edge of the reflector within the time allocated for the manoeuvre (such that $\dot{x}_m$ is proportional to the reflector size). However, for simplicity, $\dot{x}_m$ is assumed to be small and neglected; additional comments will be made at the end of this section for the general non-zero velocity case. Using these conditions, the sliding mass to reflector mass ratio can be written as:

$$\frac{m_s}{m_r} = \frac{8 l \rho_r \ddot{\beta}}{12 p_{srp} - 11 l \rho_r \ddot{\beta}} \tag{59}$$

Figure 14 shows the sliding mass as a function of the reflector size, for the three angular accelerations corresponding to a 1000, 2000 and 3000 km orbit altitude. For each angular acceleration, a maximum reflector length exists such that, given the angular acceleration $\ddot{\beta}$, the required sliding mass approaches infinity as $l \to l_{\max}$:

$$l_{\max} = \frac{12}{11} \frac{p_{srp}}{\rho_r \ddot{\beta}} \tag{60}$$

For example, for the peak angular acceleration of a 1000 km orbit the maximum reflector size according to Eq. (60) is only approximately 17 m. This value increases to approximately 236 m for a 5000 km altitude orbit. However, it should be noted that if the sliding mass dynamics are included in the analysis, the required sliding mass may increase, as

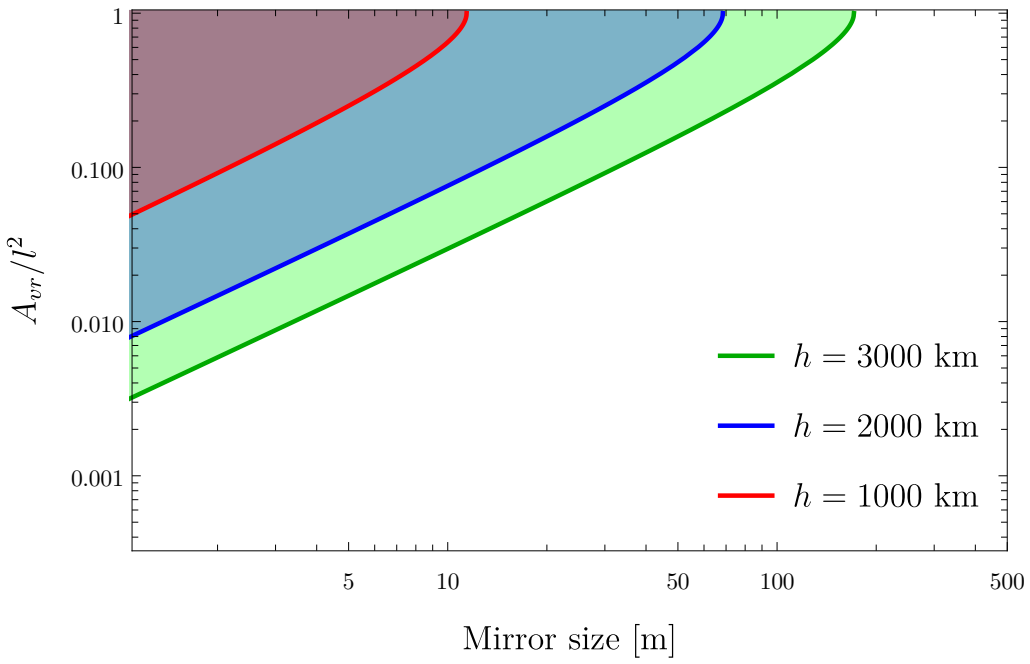

Fig. 15 Required variable reflectivity area as a function of the reflector size, for a range of angular accelerations.

suggested by Eq. (58). Furthermore, if a variable angular acceleration profile is considered, the sliding mass may be subjected to large linear accelerations, which may increase significantly the power requirements if m_s is large.

E. Variable reflectivity reflector

A net in-plane torque on the reflector can be obtained using a surface with variable reflectivity. This method has been studied extensively for solar sail applications [31, 32]. For a preliminary estimation of the achievable torque, assume that two equal rectangular regions with dimensions l and x_r along two opposite edges of the reflector can change their reflectivity, such that the resulting torque is parallel to the x_r-axis, as shown in Fig. 13b. Moreover, assume the reflectivity of these regions can be changed between 0 (completely absorbing) and 1 (completely reflecting). Then, the net torque in the x-direction is therefore:

$$T = (r_+ - r_-) p_{srp} \frac{A_{vr}}{2} \left(\frac{l}{2} - \frac{x_r}{2} \right) \cos^2 \beta \tag{61}$$

where $A_{vr} = 2x_r l$ is the total area of the two edges with variable reflectivity and r_+ and r_- are their reflectivity coefficients and the required torque is:

$$T_{required} = \frac{I_r}{2} \ddot{\beta} \tag{62}$$

Note that any additional mass required to change the reflectivity is here neglected, such that the total inertia appearing in Eq.(62) is only the inertia of the reflector. Assume that $r_- = 0$ and $r_+ = 1$ (such that the resulting torque is maximum for a given variable reflectivity area) and the angle between the reflector normal and the incoming sunlight is 45 deg. Then, solving the inequality $T \geq T_{required}$ for A_{vr} and constraining the total variable reflectivity area to be smaller than the total reflector area yields the total variable reflectivity area required to rotate the reflector with angular acceleration $\ddot{\beta}$:

$$1 - \sqrt{\frac{3p_{srp} - 4l\ddot{\beta}\rho_r}{9p_{srp}}} \leq \frac{A_{vr}}{l^2} \leq 1 \tag{63}$$

Figure 15 shows the regions where Eq. (63) is satisfied, using the same reference accelerations $\ddot{\beta}$ used in the previous section. This method is not effective for reflectors larger than 10 m for the 1000-km orbit reference acceleration. When

lower angular accelerations are allowed, larger reflectors can be used, however the required variable reflectivity area approaches the total reflector area l^2, suggesting that this type of control cannot be effective for large reflectors.

F. Current loop

This section explores the use of a current loop at the edge of the reflector to generate a torque through interaction with the Earth's magnetic field **B**. Use of current loops as secondary actuator on a 1000 m circular reflector was proposed in Ref. [10], to counteract SRP torques and desaturate CMGs. Robb et al. [16] considered distributed magnetorquers on a 100×100 m reflector and concluded that full control could be delivered if the combined areal density of the structure and magnetorquers is on the order of $10\,\mathrm{g\,cm^{-2}}$.

Consider a conductive wire at the edge of the reflector, with total length $4n_{cl}l$, where n_{cl} is the number of turns around the reflector edge. Let i be the current flowing in the circuit. The torque produced by the coil is then:

$$\mathbf{T} = \mathbf{m} \times \mathbf{B} \tag{64}$$

where $\mathbf{m} = n_{cl} i A \hat{\mathbf{k}}_r$ is the magnetic dipole generated by the current loop. Assume now a 45 deg angle between the magnetic dipole and the magnetic field and assume the output torque is parallel to the x_r-axis. The latter condition will in general not be the case for the actual reflector orbit, however it suffices to provide an approximate value of the resulting torque, so that:

$$T = \frac{\sqrt{2}}{2} n i A B \tag{65}$$

where the factor of $\sqrt{2}/2$ results from the 45 deg angle between the magnetic dipole and the Earth's magnetic field. Due to the large area enclosed within the edge of the reflector, a large control torque may be produced. A simple dipole model is used for the Earth-magnetic field:

$$B = B_0 \left(\frac{R_E}{R_o} \right)^3 \tag{66}$$

with $B_0 = 3.12 \times 10^{-5}$ T, such that $B = 2 \times 10^{-5}$ T for a 1000 km orbit. Conversely, the required torque is given by

$$T_{required} = \left(\frac{I_r}{2} + I_{cl} \right) \ddot{\beta} \tag{67}$$

where I_{cl} is the inertia of the current loop with respect to the x_r-axis:

$$I_{cl} = 2 \left[\frac{1}{12} \frac{m_{cl}}{4} l^2 + \frac{m_{cl}}{4} \left(\frac{l}{2} \right)^2 \right] = \frac{1}{6} m_{cl} l^2 \tag{68}$$

and m_{cl} is the total mass of the wire. Setting $T \geq T_{required}$ allows the minimum number of ampere-turn $n_{cl}i$ to be found:

$$n_{cl} i \geq \frac{\ddot{\beta}(m_{cl} + l^2 \rho_r)}{3\sqrt{2} B} \tag{69}$$

Given the current i and the wire resistance R the required power is then:

$$P = R i^2 \tag{70}$$

The resistance R can be written as a function of the wire resistivity ξ, its length $4nl$ and cross section A_w such that:

$$R = \xi \frac{4 n_{cl} l}{A_{cl}} \tag{71}$$

Substituting Eq. (71) into Eq. (70) and further simplifying yields:

$$P = \frac{\sigma_{cl} \xi (4l)^2}{m_{cl}} (n_{cl} i)^2 \tag{72}$$

where σ_{cl} is the density of the wire and m_{cl} is the total wire mass. Solving Eq. (72) for the ampere-turns $n_{cl}i$ and

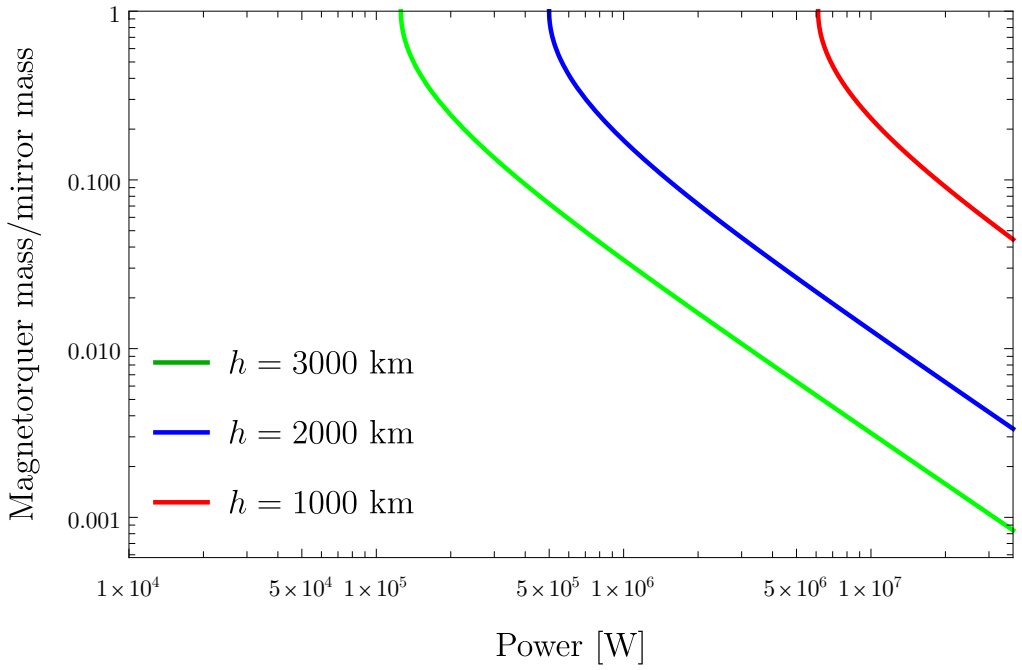

Fig. 16 Magnetorquer mass ratio as a function of the input power and orbit altitude, for $l = 1000$ m.

substituting back into Eq. (69) the required wire mass m_{cl} can be found:

$$m_{cl}^{min} < m_{cl} < m_{cl}^{max} \tag{73}$$

where:

$$\frac{m_{cl}^{min}}{m_r} = \frac{9B^2P - 16\ddot{\beta}^2 l^4 \xi \rho_r \sigma_{cl} - 3\sqrt{9B^4P^2 - 32\ddot{\beta}^2 B^2 l^4 P \xi \rho_r \sigma_{cl}}}{16\ddot{\beta}^2 l^4 \xi \rho_r \sigma_{cl}} \tag{74a}$$

$$\frac{m_{cl}^{max}}{m_r} = \frac{9B^2P - 16\ddot{\beta}^2 l^4 \xi \rho_r \sigma_{cl} + 3\sqrt{9B^4P^2 - 32\ddot{\beta}^2 B^2 l^4 P \xi \rho_r \sigma_{cl}}}{16\ddot{\beta}^2 l^4 \xi \rho_r \sigma_{cl}} \tag{74b}$$

The argument of the square root must be positive thus setting a lower bound on the required power:

$$P_{min} = \frac{32}{9} \frac{\ddot{\beta}^2 \xi \sigma_{cl} \rho_r}{B^2} l^4 \tag{75}$$

An upper bound on the available power is then given by P_{in}. By substituting Eq. (75) into Eqs. (74) it can be shown that the minimum actuator mass for $P = P_{min}$ is equal to the reflector mass, for any l. Then, m_{cl}^{min} can be reduced by increasing the supplied power P, within the range $P_{min} < P < P_{in}$. Figure 16 shows the current loop mass scaled with respect to the reflector mass, as a function of the supplied power and the orbit altitude, for a 1000 m reflector. For $h = 1000$ km a minimum power $P_{min} \approx 6$ MW is required, i.e., approximately four orders of magnitude larger than the power required by a CMG. The required power is smaller at higher orbits, although a CMG would still outperform the magnetorquer. For example, at $h = 3000$ km, $P_{min} \approx 125$ kW compared to a 1 W power requirement for a CMG at the same altitude.

G. Thrusters

Given the large specific impulses of modern electric propulsion, ion thrusters could be used to provide a large total impulse for a small propellant consumption. The torque delivered can be maximized by placing the thrusters at the edge of the reflector, while keeping the propellant tank at the center of the reflector, to minimize the increment of the

reflector's inertia due to the propellant mass. The additional inertia caused by the propellant distribution subsystem is not considered for simplicity. From the definition of specific impulse, the rate of expelled mass propellant is:

$$\dot{m} = \frac{F}{I_{sp} g_0} \tag{76}$$

where F is the net force generated by each thruster, I_{sp} is the specific impulse and g_0 is the acceleration of gravity on the Earth surface. The force F can also be written as a function of the required torque T, the number of thrusters n_t, and their distance from the rotation axis. Assuming that all thrusters are located at the edge of the reflector, i.e., at a distance $l/2$ from the rotation axis, and that the force vector is perpendicular to the reflector it follows that

$$\dot{m}_{prop} = \frac{2T}{n_t l I_{sp} g_0} \tag{77}$$

The torque T can then be written as

$$T = \frac{I_r}{2} \ddot{\beta} \tag{78}$$

where the contribution of the propellant tank on the reflector inertia has been neglected since it is close to the reflector's rotation axis (note that this approximation may not be valid for smaller structures, however it will suffice for this preliminary analysis). Therefore, the reflector inertia is approximately constant and Eq. (77) can be integrated with respect to time such that the total propellant mass during a single orbit is equal to

$$m_{prop} = n_t \int \dot{m}_{prop} dt = \frac{\int I_r |\ddot{\beta}| dt}{I_{sp} l g_0} \tag{79}$$

The numerator is the total impulse I_{tot} required for attitude control during one orbit and depends both on the tracking and reorientation accelerations. However, the reorientation phase can be neglected under the current assumption of a single PVF tracking per orbit, since the required angular acceleration is at least one order of magnitude smaller than the tracking acceleration. In case of multiple PVFs tracking per orbit this approximation may not hold and larger propellant masses may be required. It follows that:

$$I_{tot} = 2 I_r \Delta\dot{\beta}_{max} \tag{80}$$

where $\Delta\dot{\beta}_{max}$ is the maximum variation of the angular velocity during the tracking phase. The required propellant mass during a single orbit can therefore be written as

$$m_{prop} = \frac{2 I_r \Delta\dot{\beta}}{I_{sp} l g_0} \tag{81}$$

If the nominal thrust F is known, the number of thrusters n_t can then be estimated by equating the required torque with the produced torque, i.e.,

$$\frac{I_r}{2} \ddot{\beta} = n_t \frac{l}{2} F \tag{82}$$

such that

$$n_t = \frac{l^3 \ddot{\beta}}{6F} \tag{83}$$

Taking an ion propulsion system with $I_{sp} = 5000$ s and nominal thrust $F = 1$ N [6], a reflector with side $l = 1000$ m orbiting at 1000 km requires $m_{prop} = 2500$ kg and $n_t = 50$. Doubling m_{prop} to take into account additional structural mass, yields approximately 5 tonnes of material, half the mass of the reflector. Compared to other momentum exchange actuators, this option does not therefore seem attractive, not only due to the large actuator mass ratio, but also for the number of thrusters required. Note that n_t could be reduced using chemical propulsion, however, at the cost of a lower I_{sp} and therefore even larger propellant mass requirements.

V. Discussion

Table 1 summarizes the main characteristics of the actuators considered. In particular, the maximum reflector size $l_{\max}$ and the actuator mass (scaled with respect to the reflector mass) are indicated, for $h = 1000$ km and $h = 3000$

Control method	Max reflector size		Actuator to reflector mass (l = 1000 m)		Remarks
	h = 1000 km	h = 3000 km	h = 1000 km	h = 3000 km	
CMG (R_w = 1 m)	256 m (S) 1053 m (G)	477 m (S) 1936 m (G)	$\gg 1$ (S) 0.86 (G)	4.18 (S) 0.25 (G)	Low power requirement $P \approx 370$ W at 1000 km $P \approx 8$ W at 3000 km
CMG (R_w = 10 m)	820 m (S) 3330 m (G)	1509 m (S) 6123 m (G)	1.41 (S) 0.08 (G)	0.42 (S) 0.03 (G)	
RW (R_w = 1 m)	621 m (S) 2520 m (G)	1143 m (S) 4635 m (G)	2.47 (S) nd (G)	0.73 (S) 0.04 (G)	Large power requirement $P \approx 10$ MW at 1000 km $P \approx 0.7$ MW at 3000 km
RW (R_w = 10 m)	1965 m (S) 7969 m (G)	3614 m (S) $\gg 10^3$ m (G)	0.24 (S) 0.01 (G)	0.07 (S) 0.004 (G)	
Sliding masses	9 m ($m_s = m_r$) 17 m ($m_s \to \infty$)	235 m ($m_s = m_r$) 136 m ($m_s \to \infty$)	nd	nd	Not applicable to large structures
Variable reflectivity	11 m ($A_{vr} = l^2$)	161 m ($A_{vr} = l^2$)	nd	nd	Not applicable to large structures
Current loop	$> 10^3$ m	$\gg 10^3$ m	1	1	Large power requirement $P > 62$ MW at 1000 km $P > 0.13$ MW at 3000 km
Thruster	nd	nd	0.5	0.04	requires periodic propellant refilling

Table 1 Summary of mass ratio and maximum reflector length for the attitude control discussed. For momentum exchange devices, results are presented for different wheel radius R_w and material: steel (S) and graphene (G). The maximum reflector size is calculated assuming $m_w = m_r$.

km. For CMG and RW, the results are further divided based on a reference wheel radius (R_w = 1 m and R_w = 10 m) and wheel material, steel (S) and graphene (G). Also, Fig. 17 shows the maximum reflector size as a function of the orbit altitude and Fig. 18 shows the required power as a function of the reflector size and orbit altitude for CMG, RW and magnetorquer. It is apparent that CMGs can provide large torques to control very large structures, due to their low power requirements, contrary to RWs. The actuator mass can be reduced by using larger and thinner wheels or using a material with a larger specific strength. Two graphene 10 m radius wheels with a total mass of 860 kg (8% of the reflector mass) would deliver the required peak torque for a 1000 km orbit, filling a total volume of approximately 4.1 m^3. The maximum reflector size shown in the table is calculated such that the wheel mass is equal to the reflector mass. In principle, due to the low power requirements of CMGs, much larger structures could be controlled with larger power inputs (see Fig. 17, where the power constraint curves have been calculated using Eqs. (42) and (53)), however in this case the CMG mass would increase significantly and other structural issues not considered in this study may emerge at larger scales.

The CMG arrangement discussed in Section IV.A was useful to obtain analytical insights into the angular momentum and torque requirements. Clearly, different CMGs arrangements can be considered. One example, discussed in Ref. [33], involves a pair of four CMGs in a pyramid configuration, skewed at an angle of approximately 53 deg. The CMGs are mounted on the non-reflective side of the reflector. This configuration ensures redundancy and it is optimal for singularity avoidance (not considered in this analysis). Other possibilities include variable speed and/or double-gimbal CMGs [10].

Clearly, given the large wheel size requirement, the notion of a rigid graphene flywheel seems unattainable using current technology, although with the rapid development of in-orbit manufacturing this may ultimately be achievable. Alternatively, as proposed in previous NASA studies [10], deployable filamentary wheels could be used to increase the wheel radius while keeping its mass small. In Ref. [10] two 40 meter diameter CMGs are proposed to control a 1

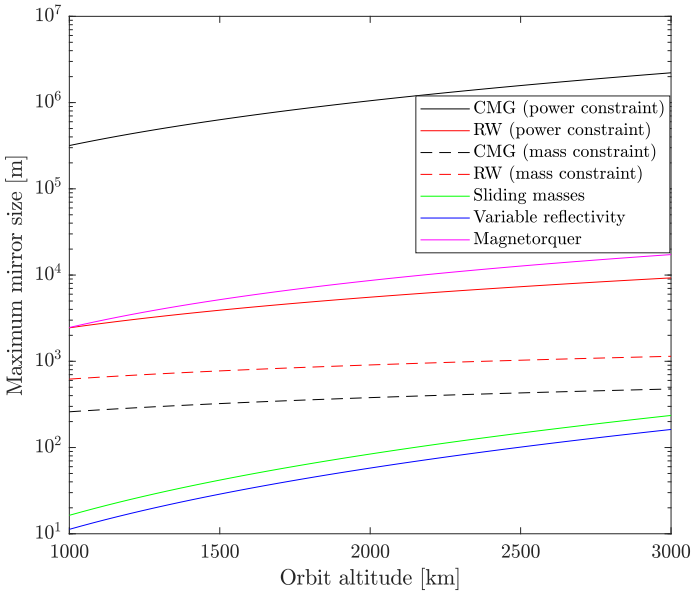

Fig. 17 Maximum reflector size as a function of the orbit altitude and the actuators considered. For CMG and RW, results are shown for steel and a wheel radius of 1 m. The mass constraint corresponds to the case $m_w = m_r$, whereas the power-constrained maximum size is calculated via Eqs. (42) and (53).

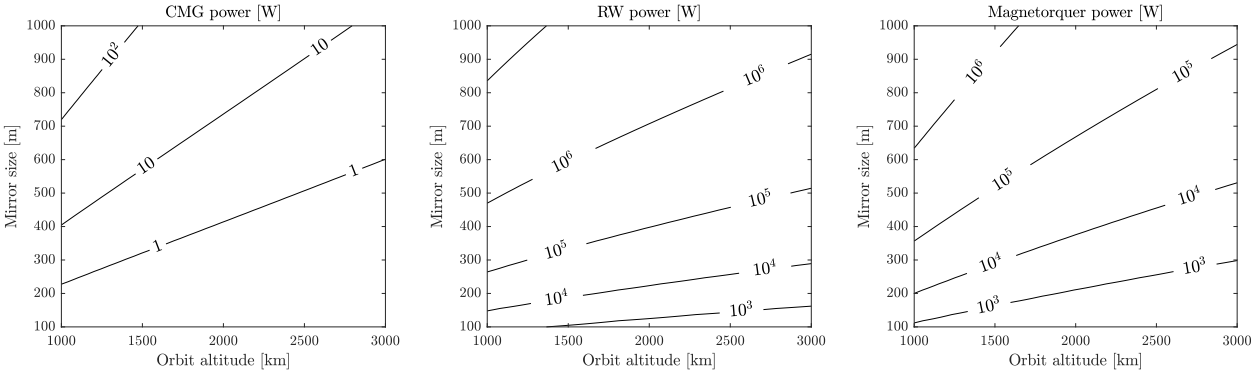

Fig. 18 Power requirements for CMG, RW and magnetorquer, as a function of the orbit altitude and reflector size.

km diameter reflector. The rotors of the CMGs are made of a fine glass fiber mesh with the fiber path chosen such that the fiber tension is constant at all locations. In addition to reducing the mass of the rotor, the advantage of this solution is that a large wheel radius can be obtained by deploying the mesh structure, which is then tensioned thanks to the centrifugal-induced forces generated by the wheel rotation. More speculatively, fluid control moment gyros could be developed, whereby a liquid is rotating inside a circular tube at the edge of the reflector, thus exchanging angular momentum without any solid rotating part [34]. As discussed in Section IV.C, using the CMGs mounted on the ISS, the maximum size of the reflector is on the order of 130 m for a 1000 km orbit.

One possible issue related to deployable CMGs or large rotors in general is the effects of CMG flexibility on the pointing accuracy. Based on the approach shown in Ref. [10] the CMGs will not cause undesirable interactions with the control system or significant pointing error if the ratio between control frequency f_c and the lowest natural frequency of the CMG f_n is smaller than 0.1. Following Refs. [10, 35] these frequencies can be estimated as

$$f_n = 0.1\frac{\omega_w}{2} \tag{84}$$

$$f_c = \frac{1}{2\pi}\sqrt{\frac{\alpha_{\max}}{\Delta\delta_e}} \tag{85}$$

where $\alpha_{\max}$ and $\Delta\delta_e$ are the maximum reflector angular acceleration and the maximum allowed pointing error, respectively. From Section III.A, the maximum reflector angular acceleration during the tracking phase can be estimated from $\ddot{\gamma}$, i.e., $\alpha_{\max} \approx \max(\ddot{\gamma}) \approx 3 \times 10^{-5}\,\mathrm{rad\,s^{-2}}$. The pointing error depends on the dimension and shape of the PVF as well as the current slant range d and can be estimated as:

$$\Delta\delta_e \approx \arctan\left(\frac{\Delta r_{\mathrm{PVF}}}{d}\right) \tag{86}$$

where Δr_{PVF} is the maximum allowed distance between the centre of the centre of the image area on the ground and the centre of the PVF. Assuming a circular PVF with a diameter of 10 km [26] and taking the slant range at $\epsilon = 0$ (i.e., at the zenith), the max pointing error is approximately 6.7×10^{-4} rad for a 1000 km orbit and 5.3×10^{-4} rad for a 3000 km orbit, where Δr_{PVF} was chosen as the radius of the PVF. Then, the ratio f_c/f_n is approximately 1.4×10^{-4} and 1.6×10^{-4} for a 1000 km and 3000 km altitude respectively, in both cases smaller than the recommended ratio of 0.1. It therefore appears that the flexibility of the CMGs will not cause significant issues with the pointing accuracy.

The SRP-based methods have a maximum controllable reflector size on the order of 10 m for an orbit altitude of 1000 km and 150 m for a 3000 km altitude. Analogous results can be obtained for other classes of SRP-based methods, such as tip-vanes [36]. This suggest that SRP cannot be used to control large reflectors at lower altitudes. However, for individually pointed reflectors connected to a frame [11], use of SRP could be a viable solution at higher altitudes, although CMGs may still be required to control the external frame.

Current loops can provide large torques, although the required mass is several orders of magnitude larger than the CMG requirement, making this solution less attractive than the CMG as a primary actuator choice. Moreover, several current loops with different orientations would be required to ensure controllability along each axis, making the resulting architecture more complex. This solution could be used as a secondary actuator for CMG desaturation or counteracting other perturbations, such as the gravity gradient torque. Considering the worse case gravity gradient torque at an orbit altitude of 1000 km, the minimum required power is on the order of 14 kW but must be increased to approximately 45 kW to decrease the wire mass below 1 tonne. For reference, each solar array wing on the ISS can produce approximately 31 kW of power [37].

One possible solution to minimize the gravity gradient torque would be to append the CMGs at the top of two booms with linear density ρ_b and length Δz, normal to the reflector, as represented in Fig. 1. The gravity gradient torque can be canceled by properly selecting the wheel mass such that $I_x = I_y = I_z$. In particular, from Eq. (28), assuming $\Delta z \gg R_w$ and $\Delta z \gg l$, the inertia of the reflector and wheel can be written as:

$$\begin{cases} I_x &\approx \dfrac{I_r}{2} + 2m_w\Delta z^2 + \dfrac{2}{3}\rho_b\Delta z^3 \\ I_y &\approx \dfrac{I_r}{2} + 2m_w\Delta z^2 + \dfrac{2}{3}\rho_b\Delta z^3 \\ I_z &\approx I_r \end{cases} \tag{87}$$

Hence, the condition $I_x = I_y = I_z$ is satisfied if

$$m_w = \frac{1}{24} m_r \left(\frac{l}{\Delta z} \right)^2 - \frac{1}{3} \rho_b \Delta z \tag{88}$$

For example, if $\Delta z = l$ and neglecting the mass of the booms, the required wheel mass would be $1/24$ of the reflector mass. In this case, the CMGs would not only provide the required tracking torque but would also cancel the gravity gradient torque. Moreover, with this configuration, the reflector rotation axis is also a principal axis, thus removing the need for torque along the y_r axis to remove the precession torque. Additional torque about the y_r axis may be required when a full three-dimensional extension of the problem is considered and the Earth rotation is taken into account. However, as discussed, the effect of Earth rotation are expected to be small at the altitudes considered here, thus the control about the y_r-axis could be accomplished with a secondary actuator such as a dedicated reaction wheel or a magnetorquer. Also note that the gravity gradient induced angular acceleration is approximately one order of magnitude smaller than the peak tracking angular acceleration at an altitude of 1000 km. Therefore, this method appears to be more attractive at higher altitudes, where the gravity gradient induced angular acceleration is comparable or larger than the tracking angular acceleration (see Fig. 9). Even if other issues related to structural stability or boom vibration may emerge, the advantages of this configuration offer scope for further investigation.

In this paper, which performs a top-level assessment of different types of actuator, the effects of the structure flexibility has not specifically been taken into account. In the case of orbiting solar reflectors, structural rigidity is essential to minimize the membrane bending or wrinkling, which may reduce the total energy delivered to the ground. In order to minimize the structure oscillations, piezo-electric actuators embedded within the structure can be used, as discussed in Ref. [15]. Alternatively, an array of small CMGs placed at optimal locations on the structure can also be used to suppress vibrations, as proposed in Refs. [13, 14]. In both cases, the additional actuators used for structural control will ultimately increase the reflector areal density, consequently increasing the torque and angular momentum requirements for the maneuver.

It is clear that more detailed analyses are required to address the optimal control architecture for each specific reflector configuration and orbit altitude, taking into account structure flexibility and vibrations, however this top-level analysis of scaling laws outlined that momentum exchange devices, in particular CMGs, can significantly reduce the actuator mass and input power requirements over other classes of actuators for control of large orbiting solar reflectors.

VI. Conclusions

In this paper, a top-level overview of actuator performance for orbiting solar reflectors in polar orbit has been presented. In particular, the attitude control requirements for pointing and reorientation maneuvers have been considered for an orbit altitude range between 1000 and 3000 km and then compared with perturbations. It has been found that the tracking requirements are dominating below an altitude of 3000 km, assuming a double-sided reflector and two reorientations per orbit. Then, based on such tracking requirements, the actuator mass and power requirements have been discussed for different classes of actuators. It has been found that control moment gyros are the most attractive actuator solution for this application. Methods based on solar radiation pressure cannot produce the required torques at large reflector scales, while magnetorquers would require very large power.

Acknowledgments

This project has received funding from the European Research Council (ERC) under the European Union's Horizon 2020 research and innovation programme (grant agreement No. 883730). CM is also supported by the Royal Academy of Engineering under the Chair in Emerging Technologies scheme.

References

[1] McRobb, M., Robb, B., Ridley, S., and McInnes, C., "Emerging space technologies: macro-scale on-orbit manufacturing," *Journal of the British Interplanetary Society*, Vol. 72, No. 12, 2019, pp. 431–434.

[2] Boyd, I. D., Buenconsejo, R. S., Piskorz, D., Lal, B., Crane, K. W., and Blanco, E. D. L. R., "On-Orbit Manufacturing and Assembly of Spacecraft," Tech. rep., Institute for Defense Analyses, 2017. URL `http://www.jstor.org/stable/resrep22854.9`.

[3] Glaser, P. E., et al., "Power from the sun: Its future," *Science*, Vol. 162, No. 3856, 1968, pp. 857–861. https://doi.org/https://doi.org/10.1126/science.162.3856.857.

[4] Schäfer, C., and Gray, D., "Transmission media appropriate laser-microwave solar power satellite system," Vol. 79, 2012, pp. 140–156. https://doi.org/10.1016/j.actaastro.2012.04.010, URL https://doi.org/10.1016%2Fj.actaastro.2012.04.010.

[5] Feingold, H., and Carrington, C., "Evaluation and comparison of space solar power concepts," *Elsevier BV*, Vol. 53, No. 4-10, 2003, pp. 547–559. https://doi.org/10.1016/s0094-5765(03)80016-4, URL https://doi.org/10.1016%2Fs0094-5765%2803%2980016-4.

[6] Wie, B., and Roithmayr, C. M., "Attitude and Orbit Control of a Very Large Geostationary Solar Power Satellite," Vol. 28, No. 3, 2005, pp. 439–451. https://doi.org/10.2514/1.6813, URL https://doi.org/10.2514%2F1.6813.

[7] Fraas, L., Palisoc, A., and Derbes, B., "Mirrors in Dawn Dusk Orbit for Low-Cost Terrestrial Solar Electric Power in the Evening," American Institute of Aeronautics and Astronautics, 2013. https://doi.org/10.2514/6.2013-1191, URL https://doi.org/10.2514%2F6.2013-1191.

[8] Oberth, H., "Ways to spaceflight," *NASA TT F-622*, 1972.

[9] Ehricke, K. A., "Space light: space industrial enhancement of the solar option," Vol. 6, No. 12, 1979, pp. 1515–1633. https://doi.org/10.1016/0094-5765(79)90003-1, URL https://doi.org/10.1016%2F0094-5765%2879%2990003-1.

[10] Hedgepeth, J. M., Miller, R. K., and Knapp, K., "Conceptual design studies for large free-flying solar-reflector spacecraft," *NASA Contractor Report, 3438*, 1981.

[11] Fraas, L. M., "Mirrors in space for low-cost terrestrial solar electric power at night," IEEE, 2012, Austin TX, USA. https://doi.org/10.1109/pvsc.2012.6318186, URL https://doi.org/10.1109%2Fpvsc.2012.6318186.

[12] Çelik, O., Viale, A., Oderinwale, T., Sulbhewar, L., and McInnes, C. R., "Enhancing terrestrial solar power using orbiting solar reflectors," *Acta Astronautica*, Vol. 195, 2022, pp. 276–286. https://doi.org/10.1016/j.actaastro.2022.03.015, URL https://doi.org/10.1016%2Fj.actaastro.2022.03.015.

[13] Hu, Q., Jia, Y., and Xu, S., "Dynamics and vibration suppression of space structures with control moment gyroscopes," *Acta Astronautica*, Vol. 96, 2014, pp. 232–245. https://doi.org/http://dx.doi.org/10.1016/j.actaastro.2013.11.032.

[14] Damaren, C., and D'Eleuterio, G., "Optimal control of large space structures using distributed gyricity," *Journal of Guidance, Control, and Dynamics*, Vol. 12, No. 5, 1989, pp. 723–731. https://doi.org/https://doi.org/10.1108/13598540610652492.

[15] Crawley, E., and De Luis, J., "Use of piezo-ceramics as distributed actuators in large space structures," *26th Structures, Structural Dynamics, and Materials Conference*, 1985, p. 626. https://doi.org/https://doi.org/10.2514/6.1985-626.

[16] Robb, B., McRobb, M., and McInnes, C., "Magnetic Attitude Control of Gossamer Spacecraft using a 3D-printed, Electrically Conducting Support Structure," *AIAA Scitech 2020 Forum, ISBN 9781624105951*, American Institute of Aeronautics and Astronautics, 2020. https://doi.org/10.2514/6.2020-0714, URL https://doi.org/10.2514%2F6.2020-0714.

[17] Robb, B., McRobb, M., Bailet, G., Beeley, J., and McInnes, C. R., "Distributed magnetic attitude control for large space structures," *Acta Astronautica*, Vol. 198, 2022, pp. 587–605. https://doi.org/https://doi.org/10.1016/j.actaastro.2022.06.045.

[18] Fu, B., Gede, G., and Eke, F. O., "Controllability of a square solar sail with movable membrane tips," *Proceedings of the Institution of Mechanical Engineers, Part G: Journal of Aerospace Engineering*, Vol. 231, No. 6, 2017, pp. 1065–1075.

[19] Choi, M., and Damaren, C. J., "Structural dynamics and attitude control of a solar sail using tip vanes," *Journal of Spacecraft and Rockets*, Vol. 52, No. 6, 2015, pp. 1665–1679.

[20] Wie, B., "Solar Sail Attitude Control and Dynamics, Part Two," *Journal of Guidance, Control, and Dynamics*, Vol. 27, No. 4, 2004, pp. 536–544. https://doi.org/10.2514/1.11133, URL https://doi.org/10.2514%2F1.11133.

[21] Borggräfe, A., Heiligers, J., Ceriotti, M., and McInnes, C. R., "Distributed Reflectivity Solar Sails for Extended Mission Applications," Springer Berlin Heidelberg, 2014, pp. 331–350. https://doi.org/10.1007/978-3-642-34907-2_22, URL https://doi.org/10.1007%2F978-3-642-34907-2_22.

[22] Larson, W. J., and Wertz, J. R., *Space mission analysis and design*, Springer, 1992. URL https://www.osti.gov/biblio/7369177.

[23] Colombo, C., and McInnes, C., "Orbital Dynamics of "Smart-Dust" Devices with Solar Radiation Pressure and Drag," Vol. 34, No. 6, 2011, pp. 1613–1631. https://doi.org/10.2514/1.52140, URL https://doi.org/10.2514%2F1.52140.

[24] Vallado, D. A., *Fundamentals of astrodynamics and applications*, Vol. 12, Springer Science & Business Media, 2001.

[25] Firuzi, S., and Gong, S., "Attitude Control of a Flexible Solar Sail in Low Earth Orbit," Vol. 41, No. 8, 2018, pp. 1715–1730. https://doi.org/10.2514/1.g003178, URL https://doi.org/10.2514%2F1.g003178.

[26] Çelik, O., and McInnes, C. R., "An analytical model for solar energy reflected from space with selected applications," *Advances in Space Research*, Vol. 69, No. 1, 2022, pp. 647–663. https://doi.org/https://doi.org/10.1016/j.asr.2021.10.033.

[27] Jacot, A. D., and Liska, D. J., "Control moment gyros in attitude control." *Journal of Spacecraft and Rockets*, Vol. 3, No. 9, 1966, pp. 1313–1320. https://doi.org/10.2514/3.28653, URL https://doi.org/10.2514%2F3.28653.

[28] Long, Z., and Zhiping, Q., "Review of Flywheel Energy Storage System," *Proceedings of ISES World Congress 2007 (Vol. I – Vol. V)*, Springer Berlin Heidelberg, 2008, pp. 2815–2819. https://doi.org/10.1007/978-3-540-75997-3_568, URL https://doi.org/10.1007%2F978-3-540-75997-3_568.

[29] King, A., Johnson, G., Engelberg, D., Ludwig, W., and Marrow, J., "Observations of Intergranular Stress Corrosion Cracking in a Grain-Mapped Polycrystal," Vol. 321, No. 5887, 2008, pp. 382–385. https://doi.org/10.1126/science.1156211, URL https://doi.org/10.1126%2Fscience.1156211.

[30] Gurrisi, C., Seidel, R., Dickerson, S., Didziulis, S., Frantz, P., and Ferguson, K., "Space station control moment gyroscope lessons learned," *Proceedings of the 40th Aerospace Mechanisms Symposium, NASA Kennedy Space Center*, 2010.

[31] Niccolai, L., Mengali, G., Quarta, A. A., and Caruso, A., "Feedback control law of solar sail with variable surface reflectivity at Sun-Earth collinear equilibrium points," Vol. 106, 2020, p. 106144. https://doi.org/10.1016/j.ast.2020.106144, URL https://doi.org/10.1016%2Fj.ast.2020.106144.

[32] Borggrafe, A., Heiligers, J., Ceriotti, M., and McInnes, C., "Attitude control of large gossamer spacecraft using surface reflectivity modulation," *65th International Astronautical Congress (IAC 2014)*, 2014, pp. IAC–14.

[33] Viale, A., Çelik, O., Oderinwale, T., Sulbhewar, L., and McInnes, C. R., "A reference architecture for orbiting solar reflectors to enhance terrestrial solar power plant output," *Advances in Space Research (submitted)*, ????

[34] Mesurolle, M., Lefèvre, Y., and Casteras, C., "Finite difference 2D model of a magnetohydrodynamic inertial actuator," *Proc. NUMELEC*, 2015, pp. 3–5.

[35] Hedgepeth, J., "Primary design requirements for large space structures," *Second AIM Conference on Large Space Platforms*, 1981.

[36] Choi, M., and Damaren, C. J., "Structural Dynamics and Attitude Control of a Solar Sail Using Tip Vanes," *American Institute of Aeronautics and Astronautics (AIAA)*, Vol. 52, No. 6, 2015, pp. 1665–1679. https://doi.org/10.2514/1.a33179, URL https://doi.org/10.2514%2F1.a33179.

[37] Davies, F., "Overview of lntemational Space Station Power System," *EnergyTech16*, 2016. URL https://ntrs.nasa.gov/api/citations/20160014034/downloads/20160014034.pdf.